Engineering Structures 370 (2027) 123973

Contents lists available at ScienceDirect

Engineering Structures

journal homepage: www.elsevier.com/locate/engstruct

A three-dimensional coupled plastic–damage–subcritical-damage–creep–shrinkage model for long-term performance of concrete structures under sustained loading

Yuan Dong [*,1], Jun Li, Shami Nejadi, Arnaud Castel

School of Civil and Environmental Engineering, University of Technology Sydney, Australia

ARTICLE INFO

Keywords:
Concrete
Plastic damage
Subcritical damage growth
Creep
Shrinkage
Three-dimensional UMAT
Long-term serviceability

ABSTRACT

Concrete members under sustained service loading can develop stiffness loss and delayed cracking below their short-term strength. This paper presents a three-dimensional creep-analysis method that couples a CDPM1-type bi-scalar plastic-damage framework with subcritical damage growth (SCG), creep, and shrinkage. Tensile and compressive damage evolve through an energy-release-rate law and a stress-activated SCG branch, creep follows a Dirichlet-series kernel fitted to AS 3600, and shrinkage is imposed as a stress-free strain; the model is implemented in Abaqus as an implicit UMAT with effective-stress return mapping, crack-band regularisation, and a consistent tangent. It is assessed against sustained flexural tests on general-purpose (GP) and GGBFS concretes: within the 280 day window GP mid-span deflections are predicted with RMSE of 0.086–0.098 mm and a maximum MAPE of 6.22%, and the same fixed SCG parameters are consistent with the slower GGBFS response, although the GGBFS data alone do not discriminate the SCG term. For the GP beams, disabling SCG shows linear creep alone cannot capture the decelerating long-term branch. The model is then applied, without recalibration, to the independent Gilbert–Nejadi benchmark — two further beams at two load levels analysed over a 300-day sustained-load window on a different section — whose measured deflections it reproduces to within about 0.3–0.6 mm. For the independent benchmark beams the SCG contribution is amplified markedly once shrinkage is active: with shrinkage disabled the subcritical increment collapses from +1.13/+0.33 mm to +0.07/+0.10 mm, as shrinkage-induced tensile stress enlarges the cracked region in which the subcritical kinetics operate. The framework thus predicts long-term serviceability deterioration under sustained flexure across the tested and benchmarked configurations.

1. Introduction

Concrete under sustained service load progressively loses stiffness and may fail even below the short-term strength, as instantaneous cracking, slow microcrack growth, creep and shrinkage couple [1,2]. Field surveys of prestressed-concrete bridges, nuclear containments and tunnel linings report decades of growing deflections, widening cracks and capacity loss [3,4]. Instantaneous plastic-damage theory cannot reproduce this: long-term assessment needs a model resolving both instantaneous plastic damage and the slow, stress-activated growth of damage under load.

The Concrete Damage Plasticity family — Lubliner et al. [5], Lee–Fenves [6], CDPM2 [7], Wu et al. [8], the CDPM1 core [9] and Mazars–Pijaudier-Cabot [10] — is standard for three-dimensional concrete cracking but essentially instantaneous: damage updates from the current state with no subcritical branch below the strength surface, so it cannot predict creep rupture, delayed crack growth or long-term stiffness loss.

Coupled creep–damage models make the compliance damage-dependent, from the one-dimensional law of Mazzotti and Savoia [11] to the 3D coupling by Ren et al. [12] of ACI 209 compliance [13] with bi-scalar damage plasticity [8]. The compliance follows empirical ACI 209 [13], fib MC2010 [14] and AS 3600 [15], and physically based Bažant B3/B4 [16], [17] and microprestress-solidification [18] models, while structural-scale studies [19–22] and [23] confirm that creep, shrinkage and damage must be coupled for serviceability. In these, time dependence rests on creep strain rather than an independent damage

* Corresponding author.
E-mail address: Yuan.Dong@student.uts.edu.au (Y. Dong).
[1] ORCID ID: 0009-0009-5014-9667

https://doi.org/10.1016/j.engstruct.2026.123973
Received 14 May 2026; Received in revised form 25 August 2026; Accepted 15 October 2026
Available online 22 October 2026
0141-0296/© 2026 The Author(s). Published by Elsevier Ltd. This is an open access article under the CC BY-NC-ND license (http://creativecommons.org/licenses/by-nc-nd/4.0/).

Nomenclature

$\bar{\sigma}$, σ	effective and nominal stress tensors	K, G	bulk and shear moduli
ε, ε_m	total and mechanical strain tensors	G_f	mode-I fracture energy
ε_e, ε_p	elastic and plastic strain tensors	h_b	characteristic element length (crack-band width)
ε_c, ε_s	creep strain tensor and shrinkage eigenstrain	ε_f	tensile softening parameter
ω^+, ω^-	net tensile/compressive bi-scalar damage variables	x_s	compressive ductility multiplier
$\omega^{\pm}_{inst}$	instantaneous (plasticity-driven) damage components	q_h, q_{h0}	hardening function and its initial value
$d_c^{\pm}$	tensile/compressive subcritical damage variables	κ_p	hardening variable
$A_s^{\pm}$	kinetic rate parameters of the SCG law	m_0, e	friction parameter and eccentricity of the yield surface
$B_s^{\pm}$	activation sensitivities of the SCG law	D_f	dilatancy parameter of the plastic potential
$k_s^{\pm}$	rate exponents of the SCG law	A_g, B_g	apex-transition parameters of the plastic potential
$d_0^{\pm}$	onset thresholds of the SCG law	$\varphi(t, \tau)$	creep coefficient at time t for loading age τ
$\varphi^{\pm}$	exponential activation functions of the SCG law	$J(t, \tau)$	creep compliance function
$\lambda^{\pm}$	normalised stress-to-strength driving ratios	$C(t, \tau)$	specific creep
f_t, f_c, f_b	uniaxial tensile, uniaxial compressive, and biaxial compressive strengths	α_i, λ_i	Dirichlet-series weights and retardation constants
		W_i	internal creep history variables
E_c, ν	concrete elastic modulus and Poisson's ratio	m	number of Dirichlet-series terms (m = 5)
		t_h	hypothetical thickness
		Δt	time increment

variable, leaving tertiary creep and delayed cracking under constant stress only partly captured.

Subcritical crack growth offers a direct route to delayed damage: from Charles [24] and Atkinson [25] and the kinetic damage-rate law of Krausz and Krausz [26], damage evolves under sustained stress below the instantaneous surface. For concrete, Wang, Le and Ren [27] used bi-scalar rate laws (reproduced in Section 2) in a Mazars/Pijaudier-Cabot framework [8], [10], and Wang, Li and Ren [28] a nano-scale fracture-kinetics rate within the parallel-bundle theory of Li and Ren [29]. Reviewed in [30], these establish subcritical growth for quasi-brittle materials but omit shrinkage and a general three-dimensional stress state.

More recently, Chianeh, Shen and Dias-da-Costa [31] embedded a time-dependent tensile-damage law in a strong-discontinuity framework with a linear B3 Kelvin chain, but confined damage to one crack-opening parameter and excluded plasticity, compressive damage and non-linear creep. No single implicit three-dimensional UMAT yet combines a CDPM1 plastic-damage core, bi-scalar tensile/compressive damage [7,8,32], subcritical growth in tension and compression [27,28], five-term Dirichlet-series creep on the effective stress [11,12] and autogenous plus drying shrinkage [13–16] for long-term assessment of reinforced-concrete members under multiaxial stress.

This paper closes that gap with a new method of three-dimensional creep analysis: a coupled CDPM1-based model implemented as an implicit Abaqus UMAT, integrating subcritical damage growth with creep and shrinkage — to the authors' knowledge the first structural-scale three-dimensional analysis method coupling all three within one plastic-damage core: existing models pair subcritical growth with creep in plane stress [27,28] or creep with time-dependent damage [33], but omit shrinkage. The bi-scalar damage of Wu et al. [8] and the Menétrey–Willam surface of Nie et al. [32] form the short-term backbone; the subcritical variables d_c^+ and d_c^- obey a kinetic law after Charles and Atkinson [24–26]; and creep, a five-term Dirichlet series fitted to AS 3600 [15] on the effective stress [12], combines with shrinkage as an eigenstrain. The study targets beam-level verification of GP-cement and GGBFS-blended concrete beams under sustained flexural loading.

Inherited are the CDPM1 plasticity surface and hardening law [9,32], the bi-scalar tensile/compressive damage split [8], the one-dimensional subcritical kinetic law and its parameters [27,28,30], the AS 3600 creep and shrinkage input [15] and the stepwise creep algorithm of the authors' prior work [34]. New here are (i) extending the bi-scalar SCG law to three dimensions through the spectral effective-stress split; (ii) integrating plasticity, bi-scalar damage, SCG, creep and shrinkage implicitly in one UMAT increment with an analytical consistent tangent, the local system reducing to a 3×3 return mapping plus a staggered scalar SCG update; and (iii) beam-level assessment against sustained-load tests on GP and GGBFS concretes and an independent benchmark, with a no-SCG counter-factual isolating the SCG contribution.

The three-dimensional formulation is deliberate. Existing subcritical- and creep-damage models for sustained loading are largely one-dimensional or plane-stress with uniaxial time-dependent strains, and to the authors' knowledge none includes shrinkage. Yet creep and shrinkage are intrinsically three-dimensional—shrinkage a volumetric eigenstrain, creep coupling stress components through Poisson effects—so their interaction with a multiaxial damage surface needs a full 3D description. In a reinforced member the reinforcement restrains free shrinkage, inducing self-equilibrated concrete tension and steel compression that beam or plane-stress elements cannot resolve yet that drive tensile damage and subcritical growth. Resolving concrete, reinforcement and bond with solid elements is therefore necessary to capture restrained-shrinkage damage and its coupling with the sustained-load flexural response—the mechanism exercised by the present tests.

2. Proposed constitutive model

The proposed model couples a three-dimensional plastic-damage core with a subcritical damage branch for time-dependent deterioration under sustained stress. The core follows the CDPM1 framework of Grassl and Jirásek [9], recast in Haigh–Westergaard coordinates by Nie et al. [32], with the tensile/compressive damage split of Wu et al. [8] replacing the single Nie–Yu factor by a bi-scalar pair (ω^+, ω^-). The subcritical branch adopts the crack-growth concept of Charles [24] and Atkinson [25] in the bi-scalar form of Wang et al. [27,28], extended here from one dimension to a general 3D return mapping.

The total strain in concrete is decomposed into elastic, plastic, creep, and shrinkage parts.

$$\varepsilon(t) = \varepsilon_e(t) + \varepsilon_p(t) + \varepsilon_c(t) + \varepsilon_s(t) \tag{1a}$$

where ε_e, ε_p, ε_c and ε_s are the elastic, plastic (CDPM1-core), Dirichlet-series creep and stress-free shrinkage strains. Fig. 1 shows the model as a series arrangement of elastic, instantaneous-damage, subcritical-damage, plastic, creep and shrinkage elements, specified below—coupled for the instantaneous plastic-damage part here and in Section 2.4 for the time-dependent part.

The stress–strain relation, Eq. (1b), uses the net tensile and compressive damage factors ω^+ and ω^- (Section 2.2), the elastic stiffness tensor D_e, the total and plastic strains ε and ε^p, and the positive and

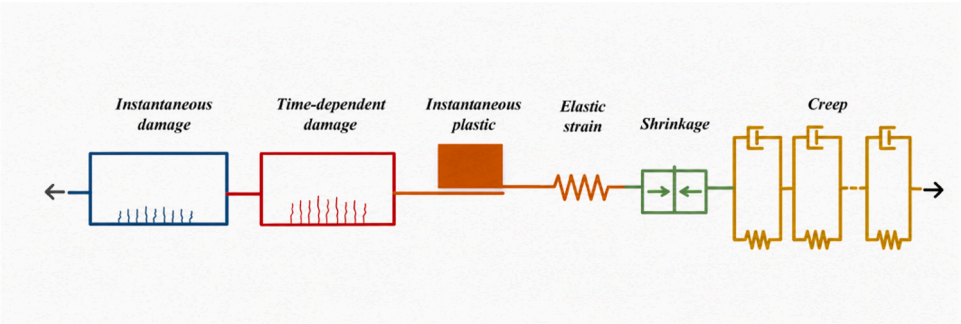


Fig. 1. Rheological schematic of the proposed model.

negative parts $\bar{\sigma}^{+}$ and $\bar{\sigma}^{-}$ of the undamaged effective stress:

$$\sigma = (1-\omega^{+})\bar{\sigma}^{+} + (1-\omega^{-})\bar{\sigma}^{-}, \bar{\sigma} = D_e : (\varepsilon - \varepsilon^{p}) \tag{1b}$$

with bulk and shear moduli

$$K = \frac{E}{3(1-2\nu)}, G = \frac{E}{2(1+\nu)} \tag{2}$$

2.1. Plasticity model

The yield surface is written in effective-stress space in Haigh–Westergaard coordinates ($\bar{\sigma}_v$, $\bar{\rho}$, θ) — hydrostatic invariant, deviatoric radius, and Lode angle:

$$\bar{\sigma}_v = \frac{I_1}{3}, \bar{\rho} = \sqrt{2J_2} \tag{3}$$

$$\theta = \frac{1}{3}\arccos\left(\frac{3\sqrt{3}J_3}{2J_2^{3/2}}\right) \tag{4}$$

The deviatoric shape is the elliptic function of Willam and Warnke,

$$r(\theta, e) = \frac{4(1-e^2)\cos^2\theta + (2e-1)^2}{2(1-e^2)\cos\theta + (2e-1)\sqrt{4(1-e^2)\cos^2\theta + 5e^2 - 4e}} \tag{5}$$

with eccentricity e from the uniaxial tensile, uniaxial compressive and biaxial compressive strengths f_t, f_c, f_b:

$$e = \frac{1+\varepsilon}{2-\varepsilon}, \varepsilon = \frac{f_t(f_b^2 - f_c^2)}{f_b(f_c^2 - f_t^2)}, f_b \approx 1.16 f_c \tag{6}$$

and the friction parameter

$$m_0 = 3\frac{f_c^2 - f_t^2}{f_c f_t}\frac{e}{e+1} \tag{7}$$

Combining Eqs. (3)–(7) with the dimensionless hardening variable q_h yields the Menétrey–Willam yield function [7,32]:

$$f_p(\bar{\sigma}_v, \bar{\rho}, \theta; q_h) = \left[(1-q_h)\left(\frac{\bar{\sigma}_v + \bar{\rho}/\sqrt{6}}{f_c}\right)^2 + \sqrt{\frac{3}{2}}\frac{\bar{\rho}}{f_c}\right]^2 + \frac{m_0 q_h^2}{f_c}\left(\bar{\sigma}_v + \frac{\bar{\rho} r(\theta, e)}{\sqrt{6}}\right) - q_h^2 \tag{8}$$

A non-associated flow rule removes the excessive dilatancy of an associated rule at high confinement [7,32]:

$$d\varepsilon^{p} = d\lambda \frac{\partial g_p}{\partial \bar{\sigma}} \tag{9}$$

with the plastic potential

$$g_p(\bar{\sigma}_v, \bar{\rho}; q_h) = \left\{(1-q_h)B_L^2 + \sqrt{\frac{3}{2}}\frac{\bar{\rho}}{f_c}\right\}^2 + q_h^2\left[\frac{m_0\bar{\rho}}{\sqrt{6}f_c}\middle| A_g B_g \exp\left(\frac{\bar{\sigma}_v - f_t/3}{B_g f_c}\right)\right], B_L = \frac{\bar{\sigma}_v}{f_c} + \frac{\bar{\rho}}{\sqrt{6}f_c} \tag{10}$$

whose apex-transition parameters A_g and B_g are calibrated from the uniaxial strengths,

$$A_g = \frac{3f_t}{f_c} + \frac{m_0}{2} \tag{11}$$

$$B_g = \frac{\frac{1}{3}(1 + f_t/f_c)}{\ln A_g - \ln(2D_f - 1) - \ln(3 + m_0/2) + \ln(D_f + 1)} \tag{12}$$

with D_f a calibrated dilatancy parameter. The hardening variable κ_p is driven by the norm of the flow vector $m = \{m_V, m_D\}^T$,

$$d\kappa_p = d\lambda\|m\| = d\lambda\sqrt{\frac{1}{3}m_V^2 + m_D^2} \tag{13}$$

where the factor 1/3 follows from $\bar{\sigma}_v = I_1/3$ in Eq. (3). The hardening function is the smooth cubic [7,9]

$$q_h(\kappa_p) = \begin{cases} q_{h0} & \kappa_p \le 0 \\ q_{h0} + (1-q_{h0})\kappa_p(\kappa_p^2 - 3\kappa_p + 3) & 0 < \kappa_p < 1 \\ 1 & \kappa_p \ge 1 \end{cases} \tag{14}$$

Fig. 2 shows the elastic domain of the Menétrey–Willam surface: the plane-stress trace (Fig. 2(a)) evolves through hardening levels $q_h = 0.6$, 0.8, 1.0, reproducing the asymmetric biaxial-compression response without a separate compression cap, while the compressive-meridian section (Fig. 2(b)) closes as a cap for $q_h < 1$ and opens into the full failure envelope at $q_h = 1$ [28]; the tensile meridian uses the same Willam–Warnke r(θ,e) of Eq. (5); the corresponding evolution of the deviatoric section during hardening is shown in Fig. 2(c).

Eqs. (1)–(14) and Fig. 2 fix the effective-stress plasticity response; the stiffness loss accompanying cracking and crushing is introduced next through the bi-scalar damage model and its subcritical-growth extension.

2.2. Damage model with subcritical damage growth

The bi-scalar damage variables ω^{+} and ω^{-} in Eq. (1b) each combine an instantaneous component $\omega_{\text{inst}}^{\pm}$ from plastic flow and a subcritical component $d_c^{\pm}$ from sustained stress through the probabilistic union [8,29].

Following Wu et al. [8], the hardening κ_p is apportioned to the tensile and compressive branches by the spectral split of the effective stress,

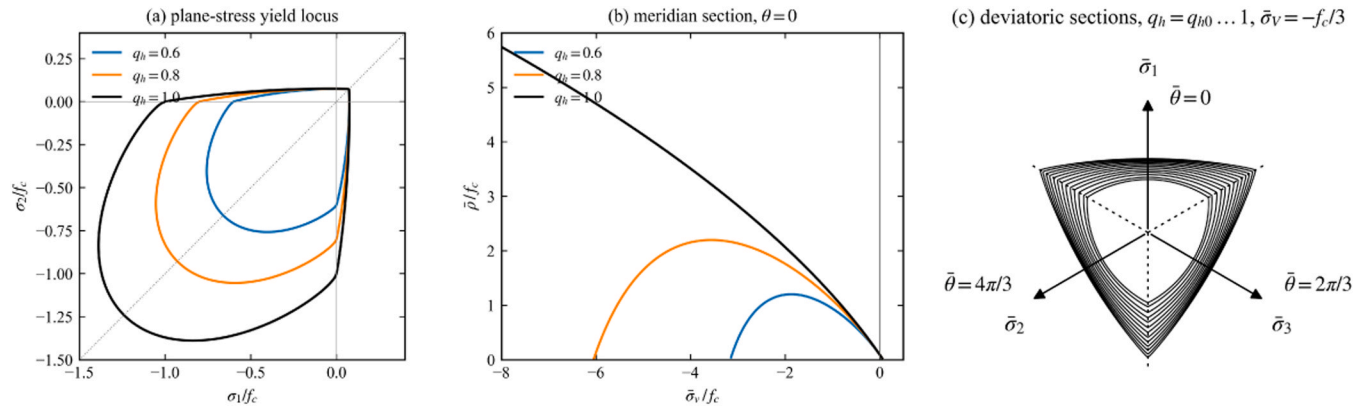


Fig. 2. Menétrey–Willam yield surface: (a) plane-stress trace; (b) compressive-meridian section; (c) evolution of the deviatoric section during hardening for a constant volumetric stress of $\bar{\sigma}V = -fc/3$.

$$w^+ = \frac{\|\bar{\sigma}^+\|}{\|\bar{\sigma}^+\| + \|\bar{\sigma}^-\|}, w^- = \frac{\|\bar{\sigma}^-\|}{\|\bar{\sigma}^+\| + \|\bar{\sigma}^-\|} \tag{15a}$$

with $w^+ = 1$ in pure tension and $w^- = 1$ in pure compression. The damage history variables are the monotone envelopes

$$\kappa_D^{\pm,n+1} = \max\left(\kappa_D^{\pm,n} | \, w^{\pm}\kappa_p^{n+1}\right) \tag{15b}$$

guaranteeing non-decreasing damage. The branches accumulate through exponential softening laws extending Nie et al.'s [32] single-scalar form to the bi-scalar case:

$$d\omega_{\text{inst}}^+ = \frac{1}{\varepsilon_f}\exp\left(|\frac{\kappa_D^+}{\varepsilon_f}\right)d\kappa_D^+, d\omega_{\text{inst}}^- = \frac{1}{x_s\varepsilon_f}\exp\left(|\frac{\kappa_D^-}{x_s\varepsilon_f}\right)d\kappa_D^- \tag{15c}$$

Integration from the virgin state $\kappa_D^{\pm} = 0$ along the monotone envelope gives the closed-form instantaneous damage factors

$$\omega_{\text{inst}}^+ = 1 - \exp\left(|\frac{\kappa_D^+}{\varepsilon_f}\right), \omega_{\text{inst}}^- = 1 - \exp\left(|\frac{\kappa_D^-}{x_s\varepsilon_f}\right) \tag{15d}$$

with tensile softening parameter ε_f and ductility multiplier $x_s > 1$ for compression. Mesh objectivity is enforced through the crack-band law [7],

$$\varepsilon_f = \frac{G_f}{h_b f_t}, h_b \le h_{b,\max} = \frac{2EG_f}{f_t^2} \tag{16}$$

where G_f is the mode-I fracture energy and h_b is the characteristic element length (the CELENT argument of the UMAT); the upper bound $h_{b,\max}$ guarantees a physically admissible softening branch.

Unlike Nie et al. [32], whose second damage branch is a low-cycle fatigue term activated on unloading, the present model repurposes it for subcritical damage under sustained loads, gated by an exponential activation function of the instantaneous damage,

$$\varphi^{\pm}(\omega_{\text{inst}}^{\pm}) = \exp\left[B_s^{\pm}\langle\omega_{\text{inst}}^{\pm} | d_0^{\pm}\rangle\right] - 1 \tag{17}$$

which vanishes below the onset threshold $d_0^{\pm}$ and grows exponentially with sensitivity $B_s^{\pm}$ above it. The driving force is the normalised stress-to-strength ratio

$$\lambda^{\pm} = \frac{\bar{\sigma}_{\text{eq}}^{\pm}}{f^{\pm} - \bar{\sigma}_{\text{eq}}^{\pm}}, \bar{\sigma}_{\text{eq}}^{\pm} = (1 - \omega_{\text{inst}}^{\pm})(1 - d_c^{\pm})\|\bar{\sigma}^{\pm}\| \tag{18}$$

with $f^+ = f_t$, $f^- = f_c$. Combining activation, driving force and rate exponent $k_s^{\pm}$ yields the subcritical damage rate law,

$$\dot{d}_c^{\pm} = A_s^{\pm}\varphi^{\pm}(\omega_{\text{inst}}^{\pm})\frac{(\lambda^{\pm})^{k_s^{\pm}}}{(1 - \omega_{\text{inst}}^{\pm})(1 - d_c^{\pm})} \tag{19}$$

in which $A_s^{\pm}$ is the kinetic rate and $(A_s | B_s | k_s | d_0)$ are defined separately for tension and compression, the denominator reflecting the decreasing effective area under damage. The parameters (Table 1) are adapted from the tensile subcritical kinetics of Wang et al. [28] and Q. Wang [30] rather than transplanted unchanged: those plain-concrete frameworks include neither restrained shrinkage nor its coupling to cracking, so the set was re-identified once for the present creep–shrinkage-coupled formulation — by inverse analysis against the measured long-term deflection histories of the in-house beams — and then held fixed — with no beam- or mix-specific re-tuning — across every analysis of Sections 5 and 6, so any compensation for unmodelled effects would surface in the independent benchmark of Section 5.5.

The complete static parameter set of the subroutine — elasticity, strength, hardening, softening and solver constants for both mixes — is consolidated in Table 15 of Appendix A.

Because the present validation targets flexural serviceability governed by tensile cracking, the compressive SCG branch is deactivated in the beam simulations ($A_s^- = 0$), isolating tensile subcritical damage under sustained bending rather than adding a compressive mechanism the present tests do not interrogate.

The four tensile SCG parameters play distinct roles: the kinetic rate A_s^+ scales the damage rate, hence long-term deflection, roughly proportionally; the activation sensitivity B_s^+ sets how sharply the branch activates once the instantaneous damage exceeds d_0^+; and k_s^+ weights highly stressed material through the driving ratio λ^+, concentrating growth near existing cracks. As they are adopted from [28,30] rather than identified for the present mixes, the one-at-a-time study of Section 6.3 quantifies each parameter's influence and bounds its effect on the long-term prediction, while independent calibration for these mixes is left as future work (Section 7).

The net bi-scalar damage factors entering Eq. (1b) follow from the

Table 1
Subcritical damage parameters.

Parameter	Value
A_s^+	1.0×10^{-5}
B_s^+	12.0
k_s^+	2.0
d_0^+	0.0
A_s^-	0.0
B_s^-	8.0
k_s^-	2.0
d_0^-	0.2

probabilistic union

$$\omega^{\pm} = 1 - (1 - \omega^{\pm}_{\text{inst}})(1 - d^{\pm}_{c}) \tag{20}$$

Hardening and bi-scalar damage combine for cyclic uniaxial loading in Fig. 3: up to peak the response follows the cubic hardening, after which ω^{+} or ω^{-} accumulates via Eq. (15c) and drives the stress to zero along the $(1 - d)E_0$ secant that sets the unloading slope. Fig. 3 verifies the inherited CDPM1 unloading/reloading response [9,32]; the present beam validation is restricted to monotonic loading followed by sustained service loading. This single-element test also serves as a basic verification of the UMAT implementation of the short-term backbone.

The damage law of Eqs. (15)–(18) and its subcritical-growth extension in Eq. (19) act on tensile and compressive components; combining them into the nominal stress first requires the effective-stress split presented next.

2.3. Stress decomposition

The effective stress is split by the spectral projection of Wu et al. [8]. The principal effective stresses, from the invariants of Eqs. (3)–(4), are

$$\bar{\sigma}_{p,1} = \bar{\sigma}_v + \sqrt{\frac{2}{3}}\bar{\rho}\cos\theta \tag{21a}$$

$$\bar{\sigma}_{p,2} = \bar{\sigma}_v + \sqrt{\frac{2}{3}}\bar{\rho}\cos(\theta - 2\pi/3) \tag{21b}$$

$$\bar{\sigma}_{p,3} = \bar{\sigma}_v + \sqrt{\frac{2}{3}}\bar{\rho}\cos(\theta + 2\pi/3) \tag{21c}$$

and the positive/negative tensors follow from the Macaulay bracket,

$$\bar{\sigma}^{+} = \sum_{i=1}^{3} \langle \bar{\sigma}_{p,i} \rangle n_i \otimes n_i, \bar{\sigma}^{-} = \bar{\sigma} - \bar{\sigma}^{+} \tag{22}$$

with n_i the unit eigenvectors of the effective stress. Substituting $\bar{\sigma}^{+}$ and $\bar{\sigma}^{-}$ with the net damage of Eq. (20) into Eq. (1b) closes the constitutive relation, delivering the nominal stress returned to global equilibrium.

2.4. Creep and shrinkage

The creep–shrinkage block follows the Stepwise Creep Incremental Analysis Method of the authors' previous work [34], referred to for the full derivation; the governing equations are reproduced here, the only addition being the subcritical-damage rate of Section 2.2, which feeds the same incremental update.

Following Eq. (1a), the mechanical strain passed to the plastic-damage update is

$$\boldsymbol{\varepsilon}_m(t) = \boldsymbol{\varepsilon}(t) - \boldsymbol{\varepsilon}_c(t) - \boldsymbol{\varepsilon}_s(t) = \boldsymbol{\varepsilon}_e(t) + \boldsymbol{\varepsilon}_p(t) \tag{23}$$

with the shrinkage $\boldsymbol{\varepsilon}_s$ added as a stress-free eigenstrain and the creep part $\boldsymbol{\varepsilon}_c(t)$ evaluated through the dimensionless elastic-compliance structure $A_{ii} = 1, A_{ij} = -\nu (i \neq j, i, j \leq 3), A_{kk} = 2(1+\nu) (k \geq 4)$ and the age- and damage-dependent compliance [34]

$$J(t, \tau, \sigma) = \frac{1 + \varphi(t, \tau)}{E_c(\tau)(1 - d(\tau))}, C(t, \tau) = \frac{\varphi(t, \tau)}{E_c(\tau)} \tag{24}$$

where $\varphi(t, \tau)$ is the creep coefficient and $d(\tau)$ the damage factor at the age of first loading. The specific creep is expanded as a Dirichlet series [34]

$$C(t, \tau) = \sum_{i=1}^{m} \alpha_i [1 - \exp(-\lambda_i (t - \tau))] \tag{25}$$

with $m = 5$ and retardation constants $\{\lambda_i\} = \{1, 10^{-1}, 10^{-2}, 10^{-3}, 10^{-4}\}\text{day}^{-1}$. The weights are obtained by a least-squares fit [34]

$$[\alpha] = (N^T N)^{-1} N^T b \tag{26}$$

of the Dirichlet expansion against the AS 3600 [15] compliance and shrinkage functions of the reference concrete, performed once off-line. As shown by Bažant and Wu [35], this exponential (Prony) series is the standard representation of creep in finite-element analysis and can reproduce any creep-compliance curve — whether code-based or obtained directly from a creep test — to arbitrary accuracy as the number of terms increases; the AS 3600 functions are targeted here rather than the cylinder creep and shrinkage tests directly for the geometrical reason set out in Section 4.2. These models take a hypothetical thickness $t_h = 2A_c/u$ evaluated separately for creep and shrinkage [34]; for creep, only the cracked compression block resists the sustained load:

$$t_{h,\text{creep}} = \frac{A_c}{u/2} = \frac{b y_{oc}}{b + y_{oc}} \tag{27}$$

where y_{oc} is the cracked-section neutral-axis depth from the transformed-section formula $y_{oc} = [-nA_{sr} + \sqrt{(nA_{sr})^2 | 2nA_{sr} db}]/b$. Shrinkage is stress-independent and evaluated on the uncracked cross-section,

$$t_{h,\text{shrinkage}} = \frac{bh}{b + h} \tag{28}$$

Creep is advanced incrementally; subtracting the creep strains at successive steps gives the recursive increment [34]

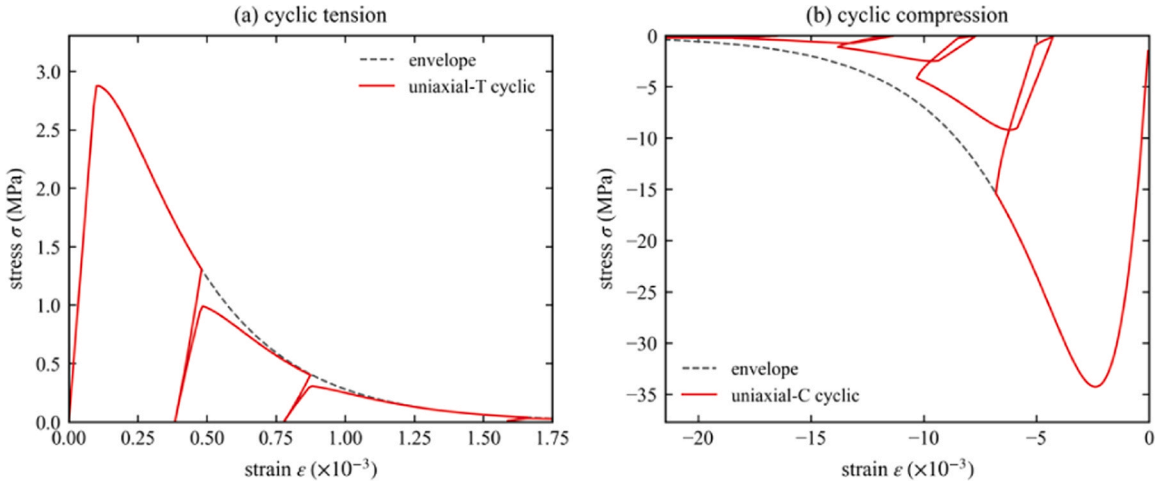


Fig. 3. Single-element cyclic uniaxial response, verifying the inherited CDPM1 unloading/reloading behaviour.

$$\Delta\boldsymbol{\varepsilon}_c(t_n) = \sum_{i=1}^{m} \alpha_i [1 - \exp(-\lambda_i \Delta t)][\boldsymbol{\sigma}(t_n) - W_i(t_{n-1})][A] \tag{29}$$

with the internal history variables W_i advanced by

$$W_i(t_n) = \exp(-\lambda_i \Delta t) W_i(t_{n-1}) + [1 - \exp(-\lambda_i \Delta t)]\boldsymbol{\sigma}(t_n) \tag{30}$$

and the elastic modulus degraded by the current damage, $E_c(t)(1-d(t))$ [34]. Only $m = 5$ scalar history variables per stress component are stored. The subcritical-damage rate of Section 2.2 enters this update through $d_c^{\pm,n+1} = d_c^{\pm,n} + \dot{d}_c^{\pm}\Delta t$, and the resulting $d_c^{\pm}$ feeds the net damage of Eq. (20), so creep, shrinkage and subcritical damage advance together in one time step.

Two clarifications are in order. First, the compliance of Eq. (24) is linear in stress: creep strains follow by superposition, with no explicit nonlinear-creep amplification of the type proposed for high sustained compressive stress [11]. This is deliberate: AS 3600 does provide a nonlinear-creep provision for high sustained compressive stress, but — like all current design codes — none for the high sustained-tension zones governing here, where the stress-level nonlinearity is instead carried by progressive tensile damage rather than creep. In the Section 4 beam programme the sustained compressive stresses stay low, where linear superposition is accepted, so the nonlinearity that matters is tensile: at high stress-to-strength ratios the SCG branch of Section 2.2 degrades stiffness through $d_c^{\pm}$, and since Eq. (24) uses the damage-degraded modulus, sustained-stress nonlinearity emerges from creep–damage coupling, not a nonlinear kernel.

Second, the storage scheme is economical, sufficient and not new: the exponential (rate-type) creep algorithm, advancing a Dirichlet/Kelvin-chain series by a recursive, history-compact update, was established by Bažant and co-workers [16,18]. The update of Eqs. (29)–(30) is exact for exponential kernels: each term advances its internal variable W_i step to step, so the full stress history need never be stored, unlike a superposition integral whose cost grows with the step count. Only one scalar per term and component ($m = 5$, i.e. 30 creep history variables per integration point) is carried. The five decade-spaced constants λ_i span retardation times from about a day to beyond the 280-day window, and the fit of Eq. (26) reproduces the AS 3600 compliance closely, so larger m would refine it only marginally.

3. Numerical implementation

The constitutive equations are integrated in an Abaqus/Standard UMAT by a staggered two-stage scheme: an implicit three-residual plastic return mapping on the Haigh–Westergaard plane, followed by a sequential update of the subcritical damage variables d_c^+ and d_c^- with the instantaneous state frozen — the operator-split architecture used with explicit updates in related subcritical and time-dependent damage models [27,28,33], the scalar rate equation here integrated by backward Euler for stability at day-scale increments. Following Nie et al. [32], the mapping uses the reduced invariants ($\bar{\sigma}_v$, $\bar{\rho}$, $\Delta\lambda$), freezing the Lode angle θ at its trial value and reducing the 7×7 Jacobian to 3×3.

3.1. Plastic return mapping

For a strain increment $\Delta\varepsilon$ and converged state at t_n, the trial effective stress is

$$\bar{\sigma}^{tr} = \bar{\sigma}_n + D_e : d\varepsilon \tag{31}$$

with components ($\bar{\sigma}_v^{tr}$, $\bar{\rho}^{tr}$, θ^{tr}) from Eqs. (3)–(4). If $f_p(\text{trial}) \le 0$ the step is elastic; otherwise the corrector updates the effective stress by

$$\bar{\sigma}_v^{n+1} = \bar{\sigma}_v^{tr} - K\Delta\lambda m_V \tag{32}$$

$$\bar{\rho}^{n+1} = \bar{\rho}^{tr} - 2G\Delta\lambda m_D \tag{33}$$

with the flow-vector components

$$m_V = \frac{\partial g_p}{\partial \bar{\sigma}_v}, m_D = \frac{\partial g_p}{\partial \bar{\rho}} \tag{34}$$

Eqs. (32), (33) and the yield condition (8) give the three-residual system

$$r = \begin{cases} r_V = \bar{\sigma}_v^{n+1} - \bar{\sigma}_v^{tr} + K\Delta\lambda m_V \\ r_D = \bar{\rho}^{n+1} - \bar{\rho}^{tr} + 2G\Delta\lambda m_D \\ r_{f_p} = f_p(\bar{\sigma}_v^{n+1}, \bar{\rho}^{n+1}, \theta^{tr}; q_h) \end{cases} \tag{35}$$

Linearising Eq. (35) in ($\bar{\sigma}_v$, $\bar{\rho}$, $\Delta\lambda$) gives the CDPM1 return-mapping Jacobian [32] (J_{33} vanishes identically):

$$J = \begin{bmatrix} 1 + K\Delta\lambda\partial m_V/\partial\bar{\sigma}_v & K\Delta\lambda\partial m_V/\partial\bar{\rho} & Km_V \\ 2G\Delta\lambda\partial m_D/\partial\bar{\sigma}_v & 1 + 2G\Delta\lambda\partial m_D/\partial\bar{\rho} & 2Gm_D \\ \partial f_p/\partial\bar{\sigma}_v & \partial f_p/\partial\bar{\rho} & 0 \end{bmatrix} \tag{36}$$

Newton iteration $\Delta x_{k+1} = \Delta x_k - J^{-1} r$ continues until $\|r\| < \text{TOL}$; the hardening variable follows Eq. (13), $\kappa_p^{n+1} = \kappa_p^n + \Delta\lambda\|m\|$, and $\bar{\sigma}^{n+1}$ passes to the damage update of Section 3.2.

3.2. Damage evolution

With $\bar{\sigma}^{n+1}$ and κ_p^{n+1} known, the instantaneous damage follows in three analytical substeps. First, the spectral decomposition of Eq. (22) splits the effective stress into positive and negative eigenparts, giving separate tensile/compressive damage. The signed plastic-strain driver follows from the energy-consistent weights

$$w^+ = \frac{\|\bar{\sigma}^+\|}{\|\bar{\sigma}^+\| + \|\bar{\sigma}^-\|}, w^- = \frac{\|\bar{\sigma}^-\|}{\|\bar{\sigma}^+\| + \|\bar{\sigma}^-\|} \tag{37}$$

which restate Eq. (15a) discretely ($w^+ = 1$ in pure tension, $w^- = 1$ in compression). Second, the split history variables advance by the monotone envelope

$$\kappa_D^{\pm,n+1} = \max\left(\kappa_D^{\pm,n} | w^{\pm}\kappa_p^{n+1}\right) \tag{38}$$

the discrete counterpart of Eq. (15b), keeping it non-decreasing under partial unloading. Third, the instantaneous damage follows from the exponential law of Eq. (15a) at the updated history

$$\omega_{inst}^{\pm,n+1} = 1 - \exp\left(-\frac{\kappa_D^{\pm,n+1}}{x^{\pm}\varepsilon_f}\right), x^+ = 1, \quad x^- = x_s \tag{39}$$

The asymmetry parameter x_s raises the compressive softening strain, delaying damage onset relative to tension, consistent with concrete's mode-dependent fracture energy [7,32]. The resulting $\omega_{inst}^{\pm}$ combine with the Section 2.2 subcritical damage through the probabilistic union (Eq. (20)), giving the net damage variables $D^{\pm}$ entering the nominal stress.

3.3. Subcritical damage update

The subcritical damage rate law of Eq. (19) is integrated implicitly over Δt; with the instantaneous damage $\omega_{inst}^{\pm}$ frozen at its plastic-corrector value, backward Euler gives the scalar residual

$$R_c^{\pm}(d_c^{\pm}) = d_c^{\pm} - d_{c,n}^{\pm} - \Delta t A_s^{\pm}\varphi^{\pm}\frac{(\lambda^{\pm})^{k_s^{\pm}}}{(1-\omega_{inst}^{\pm})(1-d_c^{\pm})} = 0 \tag{40}$$

A local Newton–Raphson iteration solves Eq. (40) with the fully analytical tangent

$$J_c^{\pm} = 1 - \Delta t A_s^{\pm}\varphi^{\pm}\left[\frac{k_s^{\pm}(\lambda^{\pm})^{k_s^{\pm}-1}(\partial\lambda^{\pm}/\partial d_c^{\pm})}{(1-\omega_{inst}^{\pm})(1-d_c^{\pm})} \middle| \frac{(\lambda^{\pm})^{k_s^{\pm}}}{(\omega_{inst}^{\pm})(1-d_c^{\pm})^2}\right] \tag{41}$$

where the driving-ratio sensitivity follows analytically from Eq. (18) as

$$\frac{\partial \lambda^{\pm}}{\partial d_c^{\pm}} = -\frac{(1-\omega_{\text{inst}}^{\pm})\|\bar{\sigma}^{\pm}\| f^{\pm}}{\left(f^{\pm}-\sigma_{\text{eq}}^{\pm}\right)^2}, \sigma_{\text{eq}}^{\pm} = (1-\omega_{\text{inst}}^{\pm})(1-d_c^{\pm})\|\bar{\sigma}^{\pm}\| \quad (42)$$

so every term in Eq. (41) is closed-form, without numerical differencing. The converged subcritical damage combines with $\omega_{\text{inst}}^{\pm}$ through Eq. (20), and the resulting $\omega^{\pm}$ enters Eq. (1b) with the spectral split of Eq. (22) to give the nominal stress σ^{n+1} and update STATEV.

3.4. Algorithmic flow

Appendix A summarises the UMAT as a flow diagram (Fig. A1), from the Abaqus strain increment through the creep–shrinkage, return-mapping, damage-update, and consistent-tangent stages to the returned nominal stress and DDSDDE, executed per Gauss point per global Newton iteration. Table 2 maps the overlined effective-stress symbols (e.g. $\bar{\sigma}$, $\bar{\rho}$) to the corresponding Fortran UMAT variables.

Both local solves use fully analytical Jacobians (Eqs. (36) and (41)), adding only a small per-Gauss-point cost. Global Newton convergence is robust but typically linear-to-superlinear. Non-converged local loops trigger reduced-step Abaqus retries (PNEWDT < 1) under the cap $j_{\max}$, i.e. solver-controlled adaptive stepping, with extra cut-backs on the high-load B1a benchmark near damage saturation. The implicit backward-Euler update (Eq. (40)) keeps the 280-day solution stable at day-scale increments, and Fig. 3 verifies the short-term backbone at element level.

4. Experimental programme

4.1. Overview of the experimental programme

Two concrete mixes were tested: a reference general-purpose cement concrete (GP) with 0.40 w/b ratio and a 50% GGBFS blended cement concrete with 0.34 w/b ratio, enabling a direct comparison of the two binder systems. Table 3 summarises the mix proportions.

Beyond the differing water-to-binder ratio, the binder composition governs hydration and pore-structure refinement, making the dataset a useful basis for comparing the GP and slag-based systems.

All specimens—cylinders and beams—were demoulded seven days after batching and stored in the laboratory for the rest of the test period; the curing and testing condition is shown in Fig. 4. Two identical beams were tested per mix. Throughout, the GP beams are designated GP2 and GP3 and the GGBFS beams GGBFS2 and GGBFS3, following the laboratory identifiers; these labels recur in the figures, tables, and error analyses of Sections 5 and 6.

Table 2
Notation.

Symbol	Description
$\bar{\sigma}$	Effective (undamaged) Cauchy stress tensor; carries the stress history before damage scaling is applied.
$\bar{\sigma}^{n}$	Effective stress at the start of the increment, recovered from STATEV.
$\bar{\sigma}^{tr}$	Trial effective stress after the elastic predictor (before plastic correction).
$\bar{\sigma}^{n+1}$	Converged effective stress at the end of the increment (after return mapping).
$\bar{\sigma}_v$	Volumetric component of $\bar{\sigma}$, $\bar{\sigma}_v = {}^1/_3\,\mathrm{tr}(\bar{\sigma})$.
$\bar{\rho}$	Norm of the deviatoric part of $\bar{\sigma}$, $\bar{\rho} = \|\mathrm{dev}(\bar{\sigma})\|$; deviatoric radius used in the yield surface.
$\bar{\sigma}_v^j$, $\bar{\rho}^j$	Newton–Raphson iterates inside the local return-mapping loop (iteration index j).
$\bar{\sigma}_{p,i}$	Principal values of $\bar{\sigma}^{n+1}$ (i = 1, 2, 3); used by the spectral split.
$\bar{\sigma}^{+}$	Tensile (positive) part of $\bar{\sigma}^{n+1}$ from the spectral split, $\bar{\sigma}^{+} = \Sigma_i \langle \bar{\sigma}_{p,i} \rangle_+ p_i \otimes p_i$.
$\bar{\sigma}^{-}$	Compressive (negative) part: $\bar{\sigma}^{-} = \bar{\sigma}^{n+1} - \bar{\sigma}^{+}$.
j, j_{max}	Newton–Raphson iteration index inside the return-mapping loop and the maximum number of iterations allowed; if j reaches j_{max} without convergence, the increment is rejected and the solver is asked to retry with a smaller step (PNEWDT < 1).

Table 3
Concrete mix design.

Components	GP (0.40 w/b)	GGBFS (0.34 w/b)
Cement	440.0	220.0
AC 20 mm	793.8	824.5
AC 10 mm	340.2	353.3
River sand	610.0	633.6
Water	176.0	149.6
GGBFS	0.0	220.0
w/b ratio	0.40	0.34
Total volume (Kg/m³)	2360.0	2401.0



Fig. 4. Curing condition.

The beam tests targeted long-term deflection growth and crack evolution under sustained loading. All beams were pre-cracked on the rig of Fig. 5 by a 40 kN load equal to the sustained load, and deflection was monitored with dial gauges. The creep coefficient and free-shrinkage strain follow AS 3600 [15] through the Dirichlet-series fit of Section 2.4, validated by companion creep and drying-shrinkage tests (Section 4.2, Fig. 6).

4.2. Material characterisation tests

A material programme measured the 28-day compressive strength and static elastic modulus of both mixes, giving the short-term references used to interpret the beam response and anchor the model inputs. Companion creep and drying-shrinkage specimens from the same batches were monitored over the sustained-load period, so the time-dependent response was measured directly. The remaining plastic-damage inputs—tensile strength, fracture-energy-related softening, and shape parameters such as q_{h0}, D_f, ε_f and x_s—are selected consistently with the adopted constitutive framework. The fracture energy, which enters only the post-peak softening through the crack-band law (Eq. 16), was calibrated once at the pre-cracking stage against the measured first-loading deflection; the computed response is in any case only weakly sensitive to its exact value within the typical normal-strength range.

Compressive strength and static chord modulus were measured to AS 1012.9:2014 and AS 1012.17–1997, respectively, on 200 mm high by 100 mm diameter cylinders. Rather than standard moist curing, the specimens were cured under the same laboratory exposure as the beams

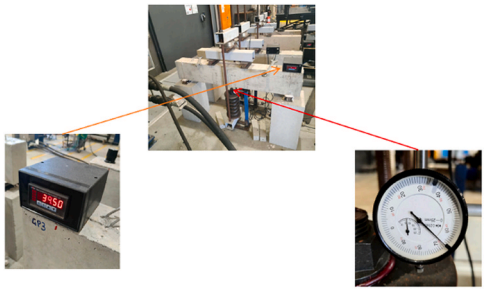


Fig. 5. Beam test setup.

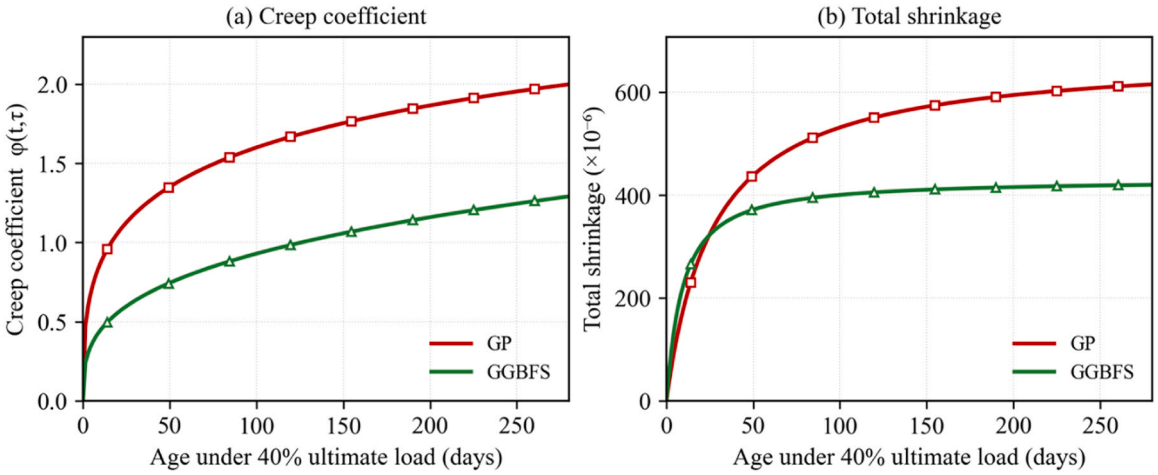


Fig. 6. Measured time-dependent material response of the GP and GGBFS concretes over the 280-day window: (a) creep coefficient under sustained load; (b) free drying shrinkage (hyperbolic fit through the measured readings).

and tested at 28 days. Replicates were tested for each mix, with individual values, average, standard deviation, and coefficient of variation (COV) reported in Table 4. The static elastic moduli are given as mix averages in the same table.

As summarised in Table 4, both mixes show low scatter (COV below 4%), and the GGBFS concrete reaches a markedly higher 28-day strength than GP, consistent with its lower w/b ratio.

The time-dependent response was measured on companion 100 mm-diameter, 200 mm-high cylinders under the same exposure. Creep under sustained load gave a creep coefficient and unloaded companions the free drying shrinkage, both monitored over the 280-day window (Fig. 6). The GP creep coefficient rises to about 2.0 against about 1.3 for the higher-strength GGBFS mix, and the drying shrinkage to about 600 microstrain for GP against 400 microstrain for GGBFS.

These curves match the AS 3600 creep and shrinkage models [15] adopted as time-dependent inputs (Section 2.4), giving direct material-level validation for both binders. They validate the code model rather than serving as beam input directly: creep and shrinkage depend strongly on the hypothetical thickness $t_h = 2A_c/u$, which for the cylinders ($t_h = 50$ mm) is far smaller than for the 150 × 250 mm beam section, so the AS 3600 model rescales the validated response to the beam geometry. The cylinder programme therefore serves as an independent cross-check on the completeness and accuracy of the beam experiments: at a common hypothetical thickness the measured material response would map directly onto the structural one, so the two scales must be mutually consistent. They are — the GGBFS creep coefficient and drying shrinkage are both measured lower than GP's, and the GGBFS beams correspondingly show the smaller long-term deflection, so this ordering reflects a measured material difference rather than an assumption from identical code inputs.

4.3. Beam test setup

All specimens share the same geometry and loading: each is 1 500 mm long with a 150 × 250 mm rectangular section, tested under four-point bending with a 400 mm constant-moment region between the loading points. This concentrates flexural cracking centrally while permitting limited shear-span cracking. The loading plan, cross-section, and longitudinal elevation appear in Fig. 7.

Reinforcement is identical across the series, so observed differences derive primarily from the mix: two N12 bottom bars, two N10 top bars, and R250 N6 stirrups; the yield strength is 550 MPa for the main bars and 250 MPa for the stirrups, with a steel elastic modulus of 200 GPa.

Both GP and GGBFS beams carried a total sustained load of 40 kN, applied as two equal 20 kN point loads and held throughout the test to track deflection growth and crack development. Each beam was simply supported on a pin and a roller, the loads placed symmetrically about mid-span to produce the constant-moment region of Fig. 7(a).

The time-dependent inputs follow the AS 3600 creep and shrinkage models [15], with Dirichlet weights from Section 2.4. These equations are applied identically to both concretes, the mix-dependent inputs being the measured strength and modulus. AS 3600 remains applicable to the GGBFS mix, as its creep and shrinkage provisions cover slag-blended cements [15] and its predictions match the Section 4.2 companion tests within scatter for both binders.

Table 4
28-day compressive strength (MPa) and static elastic modulus (GPa).

Sample	GP (0.40 w/b)	GGBFS (0.34 w/b)
1	46.3	61.8
2	43.6	57.4
3	43.3	60.9
Average	44.4	60.0
Standard deviation	1.7	2.3
COV	3.8%	3.9%
Static elastic modulus, average (GPa)	30.0	36.0

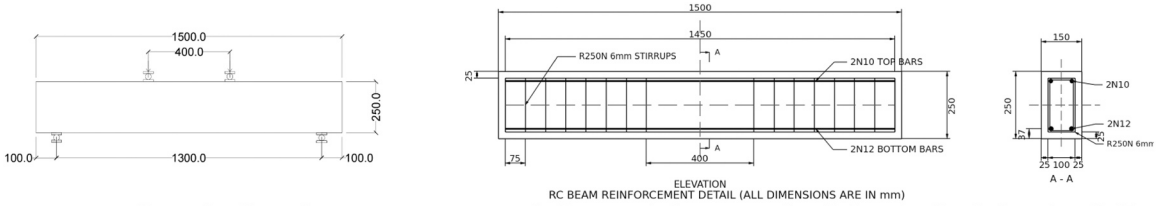
4.4. Summary of the experimental programme

Section 4.2 provides the 28-day strength and elastic-modulus references, with companion creep and drying-shrinkage measurements characterising each mix. The remaining short-term quantities in Eqs. (2), (6)–(8) and (14)–(16) follow the adopted framework, while the SCG parameters $(A_s^{\pm} | B_s^{\pm} | k_s^{\pm} | d_0^{\pm})$ in Eqs. (17)–(19) follow Wang et al. and Q. Wang and are assessed through beam-level comparison. The creep and shrinkage inputs follow AS 3600 [15], confirmed by the Section 4.2 companion tests, and enter through the Dirichlet-series fit of Section 2.4; predictions are compared with the beam measurements in Section 5.

5. Numerical verification

5.1. Finite element model

A three-dimensional FE model of the Section 4 beam programme was built in ABAQUS/Standard. Concrete used eight-noded reduced-integration hexahedra (C3D8R) with default hourglass control; longitudinal and shear reinforcement used two-noded trusses (T3D2) embedded in the concrete. The Section 2 constitutive model entered through the Section 3 UMAT, returning the stress update and consistent tangent at every integration point.



a. Beam loading plan.

b. Beam reinforcement detail: longitudinal elevation (left) and cross-section A–A (right); dimensions in mm.

Fig. 7. a. Beam loading plan. **b**. Beam reinforcement detail: longitudinal elevation (left) and cross-section A–A (right); dimensions in mm.

Boundary conditions reproduced Fig. 7a,b: pin and roller supports under four-point bending at the third points. The pin restrained vertical and longitudinal translation, the roller only vertical, avoiding artificial axial restraint during bending, creep, and shrinkage; support-line constraints suppressed out-of-plane motion. The two 20 kN loads followed the Section 4.3 history: a ramp to 40 kN, then a 280-day sustained phase. Section 2.4 Dirichlet compliance supplied creep and the AS 3600 free-shrinkage strain the eigenstrain driving the redistribution that enters the Section 2.2 subcritical-damage law.

5.2. Mesh discretisation and quality verification

The baseline model used a uniform 25 mm global element size. Mesh quality was verified with the ABAQUS Verify Mesh utility against its default criteria: quad-face corner angle below 10° or above 160°, and aspect ratio above 10. No element violated these checks, and the Shape Metrics and Analysis Checks tabs returned empty sets, so the mesh is acceptable for the global-response study.

5.3. Mesh sensitivity analysis

Mesh sensitivity of the global response and damage-zone envelope was assessed with 20, 15, and 10 mm uniform meshes (a 1:2 refinement window relative to the 25 mm baseline; Fig. 8(a–c)). Each mesh used the same loading history, with scalar damage extracted at two milestones: the instantaneous 40 kN state and the end of the 280-day sustained phase, including creep and subcritical contributions from Section 2.2. In the contours, SDV2 is short-term damage, SDV59 the long-term subcritical damage, and SDV61 their accumulated total.

The same three element sizes (20, 15 and 10 mm) are applied to the GGBFS beam of Section 4.3 with unchanged geometry, reinforcement, loading and step controls; the principal mix-dependent inputs are the measured GGBFS strength and stiffness (60.0 MPa against 44.4 MPa for GP, a 15.6 MPa increase; 36.0 against 30.0 GPa), with the remaining mix-specific constitutive constants as listed in Table 15. ABAQUS Verify Mesh flagged no elements on any of the three GGBFS meshes. Panels (d–f) of Figs. 9–11 pair the GGBFS short-, long-term and total damage with the GP panels (a–c).

Instantaneous damage at 40 kN is compared across meshes in Fig. 9 (a–c): the main flexural bands rise from the tension face in the constant-moment region and reach d ≈ 1.0, finer meshes resolving narrower bands, but the global damage zone, load–deflection branch and long-term deflection remain stable over the 10–20 mm range; the mesh-sensitivity claim concerns the global response and damage-zone envelope, not individual crack bands.

Fig. 9(a–c) is compared with the observed initial crack pattern in Table 6(b) (photographs in Table 6(a)) as a qualitative distribution check.

For GGBFS, the instantaneous damage at 40 kN Fig. 9(d–f) shows the same discrete flexural bands from the tension face as GP Fig. 9(a–c), stable across the three meshes.

The long-term field at 280 days is reported in Fig. 10(a–c). Relative to the instantaneous state, damage spreads vertically and laterally as creep redistribution and subcritical growth act, while the damaged region and global response remain stable across meshes.

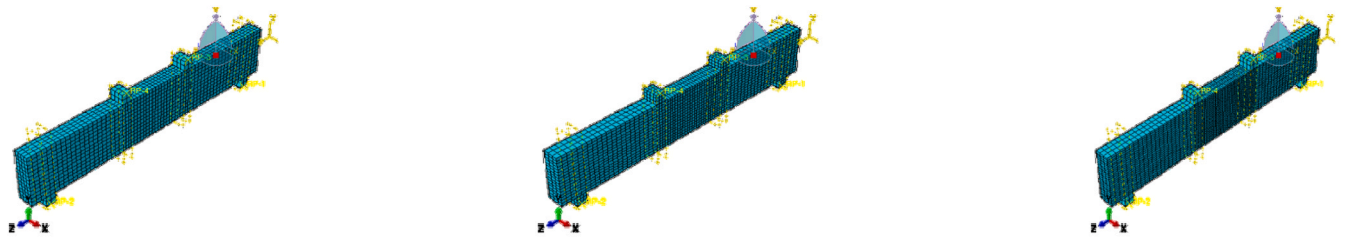
The GGBFS long-term field Fig. 10(d–f) has spread from the instantaneous state Fig. 9(d–f) but is less extensive than the GP field Fig. 10 (a–c) at the same age. With identical AS 3600 inputs, this reflects the higher GGBFS strength and stiffness, lowering the stress-to-strength ratio and hence the long-term redistribution and subcritical activation.

The total accumulated damage in Fig. 11(a–c) combines the instantaneous (Fig. 9) and long-term (Fig. 10) contributions, again supporting a stable damage-zone envelope rather than identical crack counts. For comparison with the crack maps in Table 6(b), the 15 mm and 10 mm contours resolve the observed crack density most closely.

The total GGBFS damage Fig. 11(d–f) adds localisation relative to Fig. 9(d–f) through creep redistribution and subcritical growth, while the damaged-zone location and long-term deflection stay stable across the three meshes, as for GP.

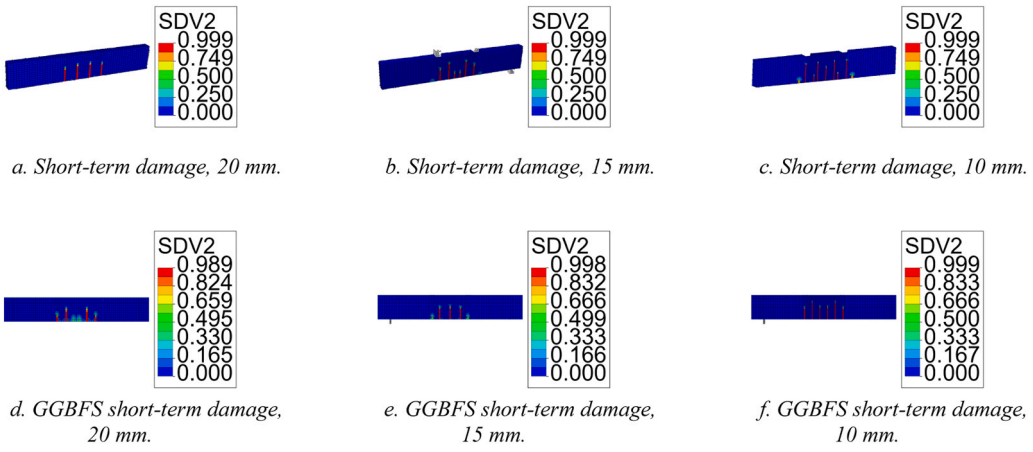
Across all three fields (Figs. 9–11), the damage-zone envelope and its concentration in the constant-moment region are preserved over the 10–20 mm range for both beams, so the 20 mm mesh is retained as the baseline for the next section.

The two behave differently under refinement: the damage contours are mesh-dependent at the level of individual crack bands, whereas the global deflection is essentially unchanged across the 10–20 mm meshes. The dependence of crack number and spacing on element size in Figs. 9–11 follows from the smeared crack-band approach: damage



a. Mesh, 20 mm. *b. Mesh, 15 mm.* *c. Mesh, 10 mm.*

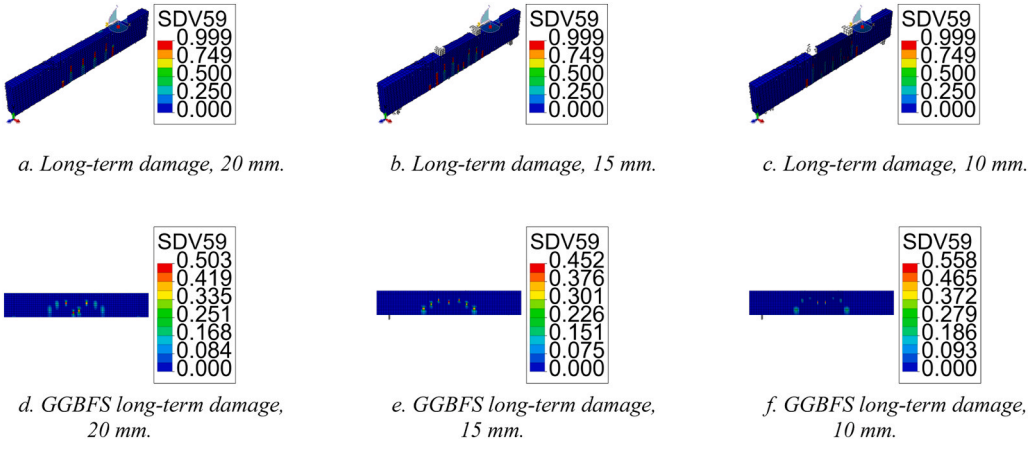
Fig. 8. a. Mesh, 20 mm. **b**. Mesh, 15 mm. **c**. Mesh, 10 mm.



a. Short-term damage, 20 mm. *b. Short-term damage, 15 mm.* *c. Short-term damage, 10 mm.*

d. GGBFS short-term damage, 20 mm. *e. GGBFS short-term damage, 15 mm.* *f. GGBFS short-term damage, 10 mm.*

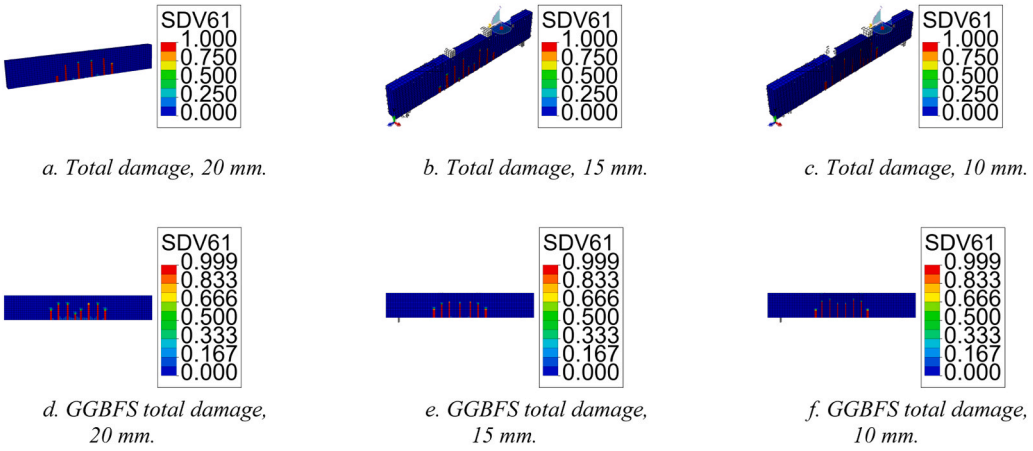
Fig. 9. a. Short-term damage, 20 mm. **b**. Short-term damage, 15 mm. **c**. Short-term damage, 10 mm. **d**. GGBFS short-term damage, 20 mm. **e**. GGBFS short-term damage, 15 mm. **f**. GGBFS short-term damage, 10 mm.



a. Long-term damage, 20 mm. *b. Long-term damage, 15 mm.* *c. Long-term damage, 10 mm.*

d. GGBFS long-term damage, 20 mm. *e. GGBFS long-term damage, 15 mm.* *f. GGBFS long-term damage, 10 mm.*

Fig. 10. a. Long-term damage, 20 mm. **b**. Long-term damage, 15 mm. **c**. Long-term damage, 10 mm. **d**. GGBFS long-term damage, 20 mm. **e**. GGBFS long-term damage, 15 mm. f. GGBFS long-term damage, 10 mm.



a. Total damage, 20 mm. *b. Total damage, 15 mm.* *c. Total damage, 10 mm.*

d. GGBFS total damage, 20 mm. *e. GGBFS total damage, 15 mm.* *f. GGBFS total damage, 10 mm.*

Fig. 11. a. Total damage, 20 mm. **b**. Total damage, 15 mm. **c**. Total damage, 10 mm. ***d****. GGBFS total damage, 20 mm.* ***e****. GGBFS total damage, 15 mm.* ***f****. GGBFS total damage, 10 mm.*

localises into bands of width h_b, and the crack-band law of Eq. (16) rescales the softening branch so the energy dissipated per unit cracked area is independent of h_b, keeping the global response objective; the band count, forming between the reinforcement-controlled stress-transfer lengths, instead follows the discretisation, so finer meshes give more and narrower bands. Since the physical crack spacing is bounded below by the bond stress-transfer length, the band count should saturate once the element size falls well below it. A 5 mm mesh was not pursued: the 15 mm and 10 mm meshes already resolve the observed crack density and shift the global response by less than the specimen-to-

specimen scatter, and band-count saturation and energy-dissipation checks on a 5 mm mesh are left to future work (Section 7).

5.4. Comparison with experiment

The model is assessed against the beam programme of Section 4.3 through the long-term mid-span deflection within the 280 day window, with FEA at the three refinement levels (10, 15, and 20 mm) of Section 5.3.

The long-term comparison is shown in Fig. 12 for both binders: GP in Fig. 12(a) and GGBFS in Fig. 12(b). The experimental data are the day-by-day mid-span deflections of beams GP2, GP3, GGBFS2 and GGBFS3 (open markers); the three mesh predictions are solver-step traces over the 0–280 day sustained phase. For both mixes the curves capture the rapid early rise and decelerating branch within the experimental band.

The contour times in Fig. 10(a–c) and Fig. 11(a–c) and the 0–280 day deflection window differ because the error statistics below use only days with paired readings; the contours are taken at the end of the GP analysis.

A quantitative error analysis is summarised in Table 5. The experimental reference is the GP2/GP3 mean at each measured day; the GP3–GP2 spread averages 0.035 mm (maximum 0.060 mm). FEA predictions are interpolated to those days, and the residuals give RMSE, MAE, MAPE, R^2, and bias. With N the number of days, y_i^{FEA} the FEA deflection interpolated to day i, y_i^{EXP} the GP2/GP3 mean on that day, and $\bar{y}^{\mathrm{EXP}}$ the temporal mean of y^{EXP}, the four indices in Table 5 are

$$\mathrm{RMSE} = \sqrt{\frac{1}{N}\sum_{i=1}^{N}\left(y_i^{\mathrm{FEA}} - y_i^{\mathrm{EXP}}\right)^2} \tag{43}$$

$$\mathrm{MAPE} = \frac{100}{N}\sum_{i=1}^{N}\left|\frac{y_i^{\mathrm{FEA}} - y_i^{\mathrm{EXP}}}{y_i^{\mathrm{EXP}}}\right| [\%] \tag{44}$$

$$R^2 = 1 - \frac{\sum_{i=1}^{N}\left(y_i^{\mathrm{FEA}} - y_i^{\mathrm{EXP}}\right)^2}{\sum_{i=1}^{N}\left(y_i^{\mathrm{EXP}} - \bar{y}^{\mathrm{EXP}}\right)^2} \tag{45}$$

$$\mathrm{Bias} = \frac{1}{N}\sum_{i=1}^{N}\left(y_i^{\mathrm{FEA}} - y_i^{\mathrm{EXP}}\right) \tag{46}$$

MAE follows the analogous absolute-residual mean. Across the three meshes the RMSE stays in the 0.086–0.098 mm range, the MAPE below 6.22%, R^2 above 0.847, and the bias magnitude is bounded by 0.054 mm. The 20 mm mesh delivers both the lowest RMSE and the lowest MAPE; all differences lie well inside the experimental scatter band, so the long-term global prediction is insensitive to mesh size over the 10–20 mm range.

Crack-pattern development is compared in Table 6 (a) and (b). The photographs and hand maps show GP cracks concentrated in the constant-moment region, sustained loading mainly extending pre-existing flexural cracks, agreeing with the FEM fields in Fig. 9(a–c) and Fig. 11(a–c): initial damage localises into vertical bands, the final total damage into a wider zone as subcritical growth and creep redistribution accumulate. The numerical bands are smoother, so the comparison is qualitative. Slow crack growth was also monitored with a fixed-focus macro camera at fixed soffit locations (Appendix B, Figs. B1 and B2); a quantitative crack-width study is left to future work (Section 7).

Table 5
GP deflection errors (97 readings, 0–280 d).

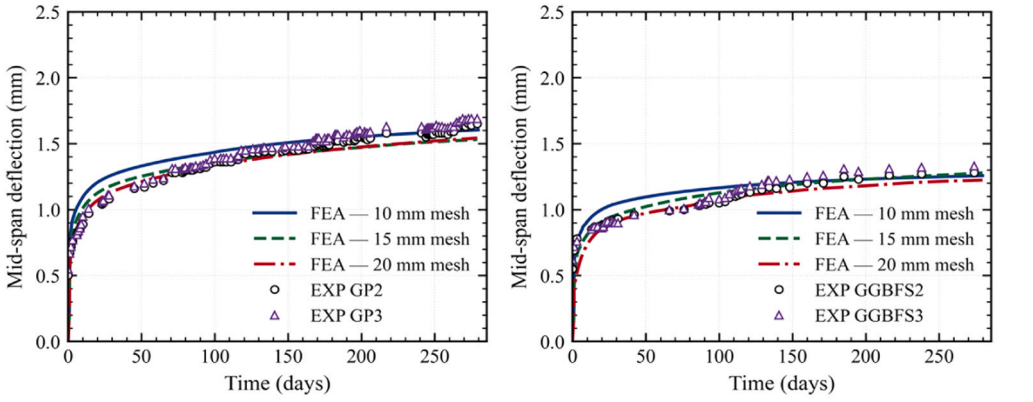
Mesh size	RMSE (mm)	MAE (mm)	MAPE (%)	R^2	Bias (mm)
10 mm	0.098	0.065	6.22	0.847	+0.040
15 mm	0.092	0.070	5.78	0.866	−0.039
20 mm	0.086	0.064	5.17	0.882	−0.054

The GGBFS beam of Section 4.3 is assessed with the same long-term deflection procedure as GP, over the 0–280 day window and the three refinement levels. The GGBFS damage fields in Fig. 10(d–f) and Fig. 11 (d–f) are reported at the end of the numerical sustained-load stage, while Table 7 uses the matched GGBFS2/GGBFS3 readings within the 0–280 day interval.

A quantitative error analysis of the GGBFS prediction is summarised in Table 7. The reference is the GGBFS2/GGBFS3 mean at each measured day; the GGBFS3–GGBFS2 spread averages 0.030 mm (maximum 0.070 mm). FEA predictions are interpolated to those days. Across the three meshes the RMSE remains in the 0.110–0.128 mm range, the MAPE below 10.25%, R^2 above 0.439, and the bias magnitude is bounded by 0.059 mm. The 15 mm mesh delivers both the lowest RMSE and the lowest MAPE; mesh-to-mesh differences lie inside the scatter band, so the long-term global GGBFS prediction is likewise insensitive to mesh size over the 10–20 mm range.

The crack-map and damage-field comparison for the GGBFS beams is given in Table 8(a) and (b). The photographs and maps show a comparatively restrained crack evolution: the dominant flexural cracks are visible from the initial stage, the final maps mainly showing extension and local widening. This matches the FEM fields in Fig. 9(d–f) and Fig. 11(d–f), where instantaneous damage concentrates near the flexural zone and total damage extends moderately after sustained loading; as for GP, the simulation gives an idealised damage envelope rather than the exact observed crack trajectories.

A direct comparison with the GP results of Section 5.4 is given in Table 9, where both error sets are reported within the 0–280-day window so that the two binders are assessed on the same footing. At the last reading in that window the GGBFS experimental mean is 1.305 mm,

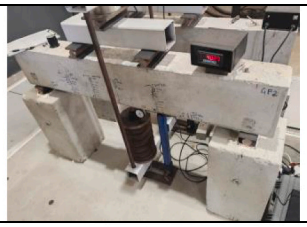
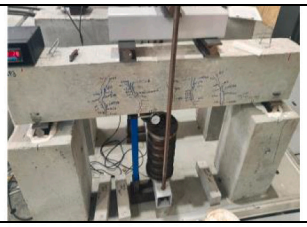


a. GP deflection: EXP vs FEA. *b. GGBFS deflection: EXP vs FEA.*

Fig. 12. a. GP deflection: EXP vs FEA. **b**. GGBFS deflection: EXP vs FEA.

Table 6
(a). GP experimental photographs. (b) GP crack maps (initial and final).

(a). GP experimental photographs.

Specimen	GP2	GP3
Experimental photograph		

(b). GP crack maps (initial and final).

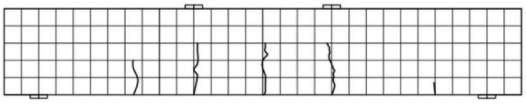
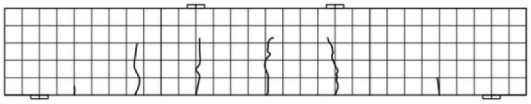
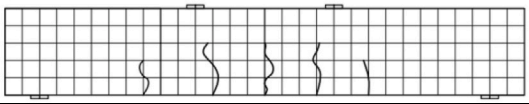
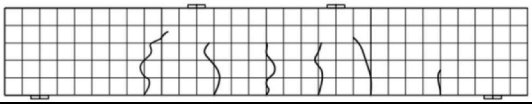
Initial crack map	Final crack map
	
	

Table 7
GGBFS deflection errors (41 readings, 0–280 d).

Mesh size	RMSE (mm)	MAE (mm)	MAPE (%)	R^2	Bias (mm)
10 mm	0.128	0.090	10.25	0.439	+0.041
15 mm	0.110	0.057	6.94	0.580	−0.008
20 mm	0.119	0.063	7.36	0.511	−0.059

against 1.670 mm for GP, so the GGBFS beam shows a long-term mid-span deflection 22% smaller under the same load. The GGBFS RMSE is 1.1–1.5 times the GP RMSE across the three meshes. The bias magnitude stays comparable between mixes (within 0.059 mm for GGBFS, within 0.054 mm for GP), so the comparison is governed by the absolute residual and specimen scatter rather than a systematic shift.

This reduction should be read against the AS 3600 input model, whose creep and shrinkage equations are common in form to both concretes with no explicit binder-composition factor. The dominant difference in this dataset is the much higher GGBFS compressive strength (60.0 MPa against 44.4 MPa for GP, a 15.6 MPa increase) and associated stiffness. The strength enters the AS 3600 equations directly, giving GGBFS a lower creep coefficient and lower shrinkage — consistent with its independently measured lower drying shrinkage (Section 4.2) — and, together with the stiffness, lowers the stress-to-strength ratio under the same load, restraining the redistribution and SCG activation driving the long-term branch.

Table 8
(a). GGBFS experimental photographs. (b) GGBFS crack maps (initial and final).

(a). GGBFS experimental photographs.

Specimen	GGBFS2	GGBFS3
Experimental photograph		

(b). GGBFS crack maps (initial and final).

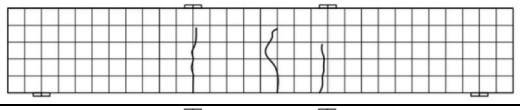
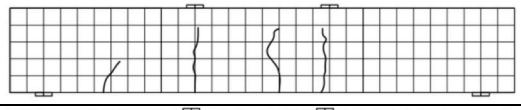
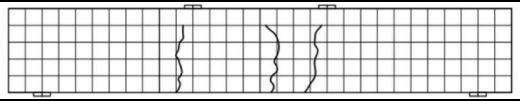
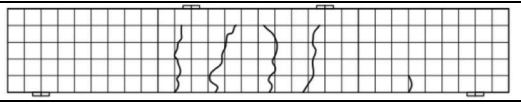
Initial crack map	Final crack map
	
	

Table 9
GP/GGBFS deflection errors (0–280 d).

Mix	Mesh size	n	RMSE (mm)	MAE (mm)	MAPE (%)	R^2	Bias (mm)
GP	10 mm	97	0.098	0.065	6.22	0.847	+0.040
	15 mm	97	0.092	0.070	5.78	0.866	−0.039
	20 mm	97	0.086	0.064	5.17	0.882	−0.054
GGBFS	10 mm	41	0.128	0.090	10.25	0.439	+0.041
	15 mm	41	0.110	0.057	6.94	0.580	−0.008
	20 mm	41	0.119	0.063	7.36	0.511	−0.059

5.5. Independent validation against an external sustained-load benchmark

To broaden the empirical basis beyond the in-house GP and GGBFS programme, the model was applied, with its literature parameter set unchanged and no benchmark-specific re-tuning, to the independent sustained-load reinforced-concrete beams of Gilbert and Nejadi [36], adding two load levels, a different cross-section and reinforcement layout, and a longer observation window. The nominally identical beams B1a and B1b differ only in sustained-load level. Each spans 3500 mm with a 250 × 348 mm section (effective depth 300 mm) reinforced by two N16 tensile bars ($A_s \approx 402$ mm^2, $E_s = 200$ GPa), third-point loaded and sustained from an age of 14 days; B1a carries 18.6 kN and B1b 11.8 kN per point. The measured mid-span deflection grows from 4.97 to about 12 mm at 380 days (B1a) and from 2.24 to 7.3 mm (B1b).

Both beams (Fig. 13) used the constitutive routine and conventions of Section 5.1: a half-width symmetric Abaqus/Standard model (C3D8R concrete with embedded T3D2 truss reinforcement, ≈ 20 mm elements, about 17 900 in total), a pre-crack step ramping the sustained load at an equivalent age of 14 days, and a 300-day sustained step capped at a one-day increment. The age-dependent elastic modulus (22.8 → 25.0 GPa) and tensile strength (2.0 → 2.8 MPa) follow the measured maturation, and the AS 3600 creep coefficient ($\varphi_\infty \approx 1.7$) and drying-shrinkage strain (≈ 825 microstrain) use the same Dirichlet-series kernels as before.

A uniform-mesh convergence check supports this ≈ 20 mm choice. Beam B1b was re-analysed with three uniform element sizes — 20, 25 and 30 mm (17 922, 9 940 and 5 684 elements over the symmetric half-width; C3D8R concrete with embedded T3D2 reinforcement) — under otherwise identical settings. The 300-day mid-span deflection is 7.124, 7.127 and 5.586 mm respectively (Fig. 14b): refining from 25 to 20 mm shifts it by only 0.003 mm, whereas the coarse 30 mm mesh under-predicts by about 1.54 mm (≈ 22%). The smeared tensile-damage band likewise converges at 25 mm and finer, each element carrying a single cracked column, consistent with the crack-band regularisation of the softening law, so the coarse mesh both spreads the localisation and loses deflection; the damage-field comparison (Fig. 15) shows the same flexural crack band on every mesh, resolved by fewer, wider smeared cracks as it coarsens. The 20 mm discretisation is retained for all production runs. The B1a mesh study is likewise extended over three uniform element sizes — 20, 25 and 30 mm — run to 300 days: the 300-day mid-span deflection changes from 11.28 mm on the 20 mm mesh to 11.27 mm on the 25 mm mesh, a 0.1% difference, while the coarser

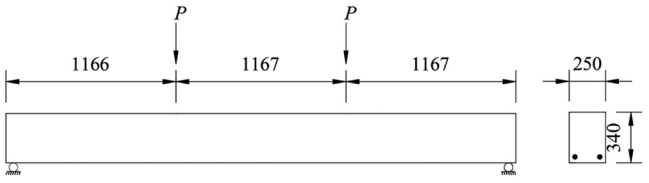


Fig. 13. Gilbert and Nejadi benchmark beams: elevation with the two third-point sustained loads on a simply supported 3500 mm span, and cross-section (dimensions in mm).

30 mm mesh gives 10.01 mm, about 11% lower (Fig. 14a); the response is therefore converged between the 20 and 25 mm meshes, with the 30 mm mesh too coarse to resolve the crack-band contribution. On the 25 mm mesh the instantaneous deflection of 4.41 mm grows by a further 6.86 mm (156%) over 300 days, and the net tensile-damage crack band is preserved on the finer 20 and 25 mm meshes (Fig. 15a,b), confirming that the B1a conclusions are likewise mesh-insensitive.

The predicted and measured mid-span deflection histories are compared in Fig. 14. The full model tracks the measured response closely: at 300 days it gives 11.28 mm (B1a) and 7.12 mm (B1b) against measured 11.69 and 7.25 mm (Table 13), and the day-by-day residual over 20–300 days stays within −0.6–0 mm for B1a and about ±0.3 mm for B1b (Table 10). As in-house, the model slightly under-predicts the very short-term deflection, but this closes within about 30 days and does not affect the decelerating long-term branch.

The tensile-damage field of the more heavily loaded B1a is shown in Fig. 16: tensile damage at first loading (Fig. 16a), and at 300 days the damage contributed by subcritical growth (Fig. 16b) and the net tensile damage (Fig. 16c). Discrete flexural cracks form in the constant-moment region on loading, and under the higher B1a load the net tensile damage there grows towards the damage cap by the end of the step. As the damage approaches unity the saturated band's tangent stiffness becomes near-singular and the equilibrium path develops a snap-back limit point driving the time increment to zero; convergence to 300 days is maintained by adaptive cut-backs of the automatic time incrementation. The damage cap and the accompanying freeze of the subcritical updates act only as a bound on the damage internal state variables once the cap is reached, with negligible effect on the macroscopic deflection.

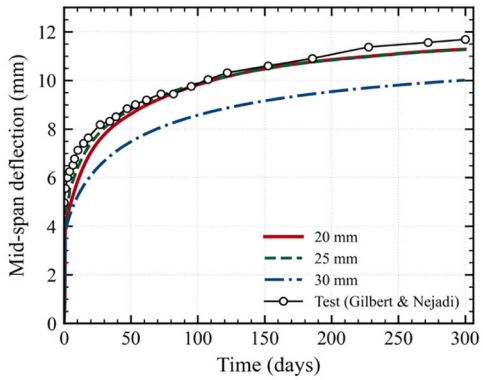
The corresponding fields of the lightly loaded B1b are shown in Fig. 17. The flexural crack band again forms in the constant-moment region at first loading, but under the lower load the net tensile damage at 300 days stays well below saturation (Fig. 17c), so the snap-back regularisation is exercised only by B1a.

The simulated damage bands are compared with the observed crack patterns in panels (d) of Fig. 16 and Fig. 17, the soffit crack maps reported by Gilbert and Nejadi [36]. In both experiment and model the flexural cracks are confined to the constant-moment third of the span at a regular spacing set by the reinforcement bond, and the more heavily loaded B1a develops denser cracking than B1b — the same trend shown by the predicted tensile-damage bands of Fig. 16 and Fig. 17. The comparison is qualitative but consistent with the model localising damage in the correct region and reproducing the observed load-dependence.

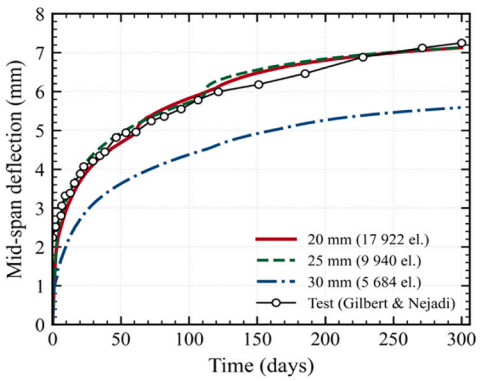
6. Role of subcritical damage growth

6.1. GP and GGBFS beam counter-factual

The Section 5.4 deflection traces do not separate the Section 2.2 subcritical damage growth (SCG) term from the Section 2.4 linear creep convolution. To isolate it, the Section 4.3 beam programme was re-run with SCG switched off in the UMAT ($\dot{d}_c^+ = \dot{d}_c^- = 0$), leaving linear creep as the only time-dependent mechanism; mesh, loading, plasticity, and instantaneous damage are unchanged. The ablation is restricted to the newly proposed SCG term: the instantaneous damage cannot be removed independently, since the SCG branch is gated by it through the activation function of Eq. (17), so zeroing it also suppresses the SCG contribution. Creep and shrinkage are code-based inputs validated in Section 4.2. A recalibrated nonlinear-creep baseline is not a meaningful alternative here: established nonlinear-creep laws amplify the compressive creep compliance at stress ratios above about 0.4 f_c, which the compression zone of these beams never approaches at service load, whereas in the cracked tension zone — where the long-term nonlinearity actually resides — no accepted tensile nonlinear-creep calibration exists, and the stress-level-dependent time effect is precisely what the subcritical term represents mechanistically. Fitting such a baseline to the



a. B1a (18.6 kN): mesh sensitivity and measured vs predicted (20/25/30 mm).



b. B1b (11.8 kN): mesh sensitivity and measured vs predicted (20/25/30 mm).

Fig. 14. a. B1a (18.6 kN): mesh sensitivity and measured vs predicted (20/25/30 mm). **b**. B1b (11.8 kN): mesh sensitivity and measured vs predicted (20/25/30 mm).

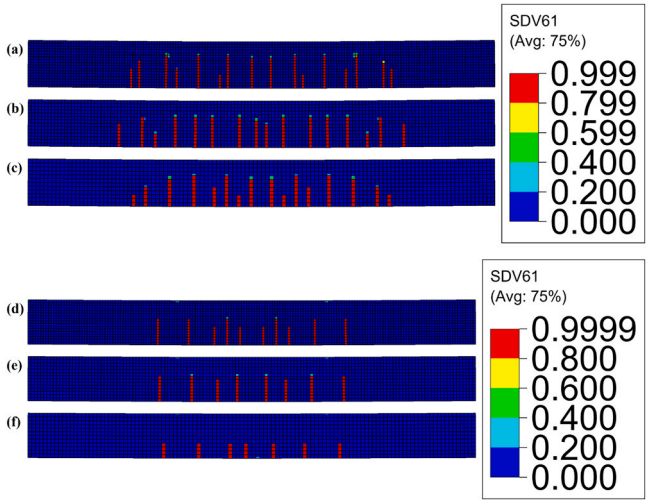


Fig. 15. Mesh sensitivity of the net tensile-damage field at 300 days: beam B1a on the (a) 20 mm, (b) 25 mm and (c) 30 mm meshes, and beam B1b on the (d) 20 mm, (e) 25 mm and (f) 30 mm meshes.

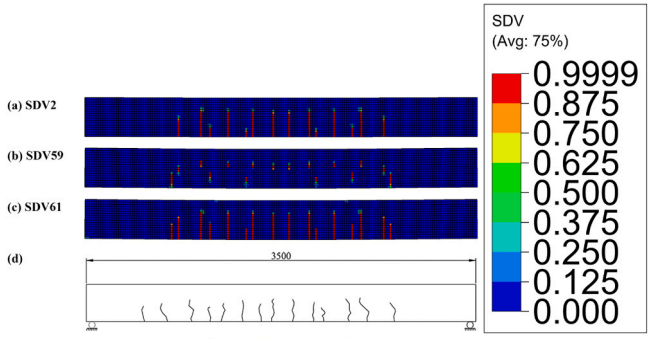


Fig. 16. Predicted tensile-damage fields of beam B1a: (a) tensile damage (SDV2) at first loading (sustained-load day 0), with discrete flexural cracks in the constant-moment region; (b) tensile damage contributed by subcritical growth (SDV59) at 300 days; (c) net tensile damage (SDV61) at 300 days; (d) observed crack pattern (after Gilbert and Nejadi).

Table 10
Independent benchmark (Gilbert and Nejadi): long-term mid-span deflection error of the full model against the measured response over the 20–300-day window, using the error metrics of Eqs. (43)–(46).

Beam	N	RMSE (mm)	MAE (mm)	MAPE (%)	R^2	Bias (mm)
B1a	15	0.282	0.236	2.52	0.927	−0.233
B1b	17	0.169	0.148	2.89	0.969	+0.016

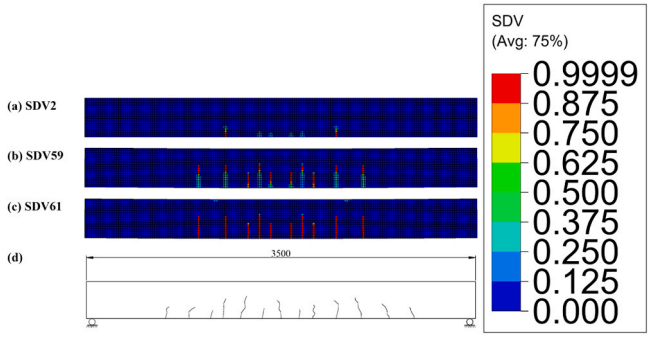


Fig. 17. Predicted tensile-damage fields of beam B1b: (a) tensile damage (SDV2) at first loading (sustained-load day 0); (b) tensile damage contributed by subcritical growth (SDV59) at 300 days; (c) net tensile damage (SDV61) at 300 days; (d) observed crack pattern (after Gilbert and Nejadi).

same beam deflections it is meant to test against would be circular.

By construction the two analyses share the same full-load state: short-term damage, elastic-plastic stress, and service-load deflection are fixed by Sections 2.1–2.2, where no SCG terms appear, so the two deflections coincide at the first sustained day and diverge only as SCG accumulates damage.

The two cases are compared mesh-by-mesh in Fig. 18(a–c), with the GP2/GP3 points overlaid. For every mesh the with-SCG curve lies above the no-SCG curve: SCG adds damage where stress lies below short-term strength but above the subcritical onset threshold, reducing bending rigidity beyond linear creep.

The SCG impact is summarised in Table 11. With SCG the error against the GP2/GP3 mean stays essentially mesh-insensitive: RMSE 0.086–0.098 mm, MAPE below 6.22%, and R^2 above 0.847. Without SCG the RMSE rises to 0.232 mm, the MAPE to 14.48%, and R^2 drops to 0.138, with uniformly negative bias. At the last measured day the two predictions differ by 0.072 mm (10 mm) and 0.240 mm (20 mm), against an experimental mean of 1.670 mm; the no-SCG prediction falls outside the GP2/GP3 band, the with-SCG prediction inside it, so linear creep alone cannot reproduce it.

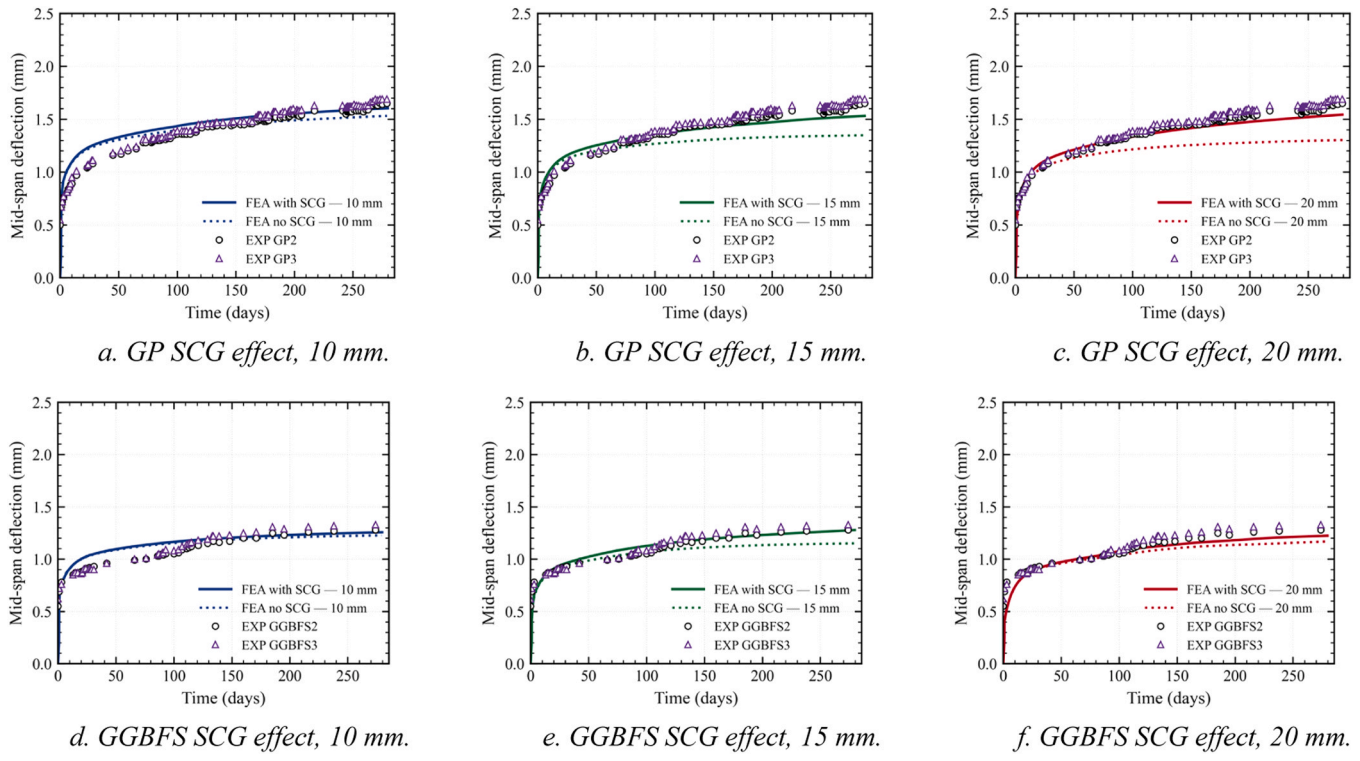


Fig. 18. a. GP SCG effect, 10 mm. **b**. GP SCG effect, 15 mm. **c**. GP SCG effect, 20 mm. **d**. GGBFS SCG effect, 10 mm. **e**. GGBFS SCG effect, 15 mm. **f**. GGBFS SCG effect, 20 mm.

Table 11
GP SCG ablation (0–280 d).

Mesh size	Case	RMSE (mm)	MAPE (%)	R^2	Bias (mm)	Defl. (last d, mm)
10 mm	with SCG	0.098	6.22	0.847	+0.040	1.603
	no SCG	0.103	6.89	0.830	−0.009	1.531
15 mm	with SCG	0.092	5.78	0.866	−0.039	1.531
	no SCG	0.191	11.99	0.412	−0.149	1.348
20 mm	with SCG	0.086	5.17	0.882	−0.054	1.543
	no SCG	0.232	14.48	0.138	−0.205	1.303

Two observations follow. First, SCG controls the decelerating branch: zeroing it collapses R^2 from above 0.847–0.138, and the final deflection falls short. Second, no-SCG residuals grow with element size whereas with-SCG residuals remain essentially mesh-insensitive in the sense of Section 5.3, so the long-term predictive capability comes from the SCG kinetics, not crack-band regularisation alone.

The same ablation is repeated on the GGBFS beam of Section 4.3, with the same UMAT switch ($\dot{d}_c^{+} = \dot{d}_c^{-} = 0$) and three meshes, over the matched GGBFS2/GGBFS3 readings in the 280-day window.

The two cases are compared mesh-by-mesh in Fig. 18(d–f) over the 280-day sustained phase, with GGBFS2/GGBFS3 overlaid. The with-SCG curve again lies at or above the no-SCG curve, but the separation is much smaller than for the GP beam of Fig. 18(a–c): at the last measurement day inside the 280-day window the with- and no-SCG predictions differ by 0.029 mm on the 10 mm mesh, 0.125 mm on the 15 mm mesh, 0.055 mm on the 20 mm mesh, against 0.072 mm, 0.184 mm, 0.240 mm for the GP beam.

The GGBFS SCG impact over the 280-day window is summarised in Table 12. With SCG the error against the GGBFS2/GGBFS3 mean is essentially mesh-insensitive: RMSE 0.110–0.128 mm, MAPE below 10.25%, R^2 above 0.439, and bias within 0.059 mm. Without SCG the RMSE moves to 0.124–0.132 mm, the MAPE to 10.15%, R^2 to 0.404, and bias within 0.084 mm. The largest with-/without-SCG RMSE gap on any GGBFS mesh is thus 0.014 mm, against 0.146 mm on the worst GP mesh of Table 11.

Read against the GP results of Table 11, two points emerge. First, switching SCG off affects GGBFS far less than GP: removing it collapses GP R^2 from above 0.847 to about 0.138, whereas the GGBFS R^2 moves only from 0.439 to 0.404 and the error ranges stay close. The GGBFS no-SCG bias remains within 0.084 mm of zero, against an order-of-magnitude larger GP no-SCG bias (up to 0.205 mm). Second, the SCG contribution scales with the underlying deflection: the stiffer GGBFS beam deflects less, with a smaller SCG-induced separation (mean at the last day 0.070 mm against 0.165 mm for GP).

These observations are consistent with Section 2.2: the SCG rate is gated by instantaneous damage and driven by normalised stress-to-strength ratio, both smaller in the higher-strength GGBFS beam under

Table 12
GGBFS SCG ablation (0–280 d).

Mesh size	Case	RMSE (mm)	MAPE (%)	R^2	Bias (mm)	Defl. (last d, mm)
10 mm	with SCG	0.128	10.25	0.439	+0.041	1.255
	no SCG	0.126	10.15	0.454	+0.031	1.226
15 mm	with SCG	0.110	6.94	0.580	−0.008	1.275
	no SCG	0.124	7.90	0.471	−0.058	1.150
20 mm	with SCG	0.119	7.36	0.511	−0.059	1.221
	no SCG	0.132	9.16	0.404	−0.084	1.166

the same 40 kN sustained load. The AS 3600 creep and shrinkage functions are kept identical for both concretes, with no binder-specific slag model, and the SCG parameters are reused unchanged; the response changes only through the instantaneous stress state and strength.

In summary, the GGBFS comparison is consistent with, but does not by itself confirm, the model: because the with-SCG and no-SCG predictions are close for this higher-strength mix, the GGBFS data mainly constrain the creep–shrinkage backbone rather than the SCG kinetics, so the SCG parameters are not independently shown transferable to GGBFS here. The smaller SCG impact matches the lower damage-driving ratio under the same load, and the companion tests of Section 4.2 give the GGBFS mix a measured drying shrinkage well below the GP mix (about 370–450 against 600–670 microstrain), so the much smaller and slower deflection increase is the result of a genuine material difference. It is thus a higher-strength, lower-shrinkage response, to be re-examined at longer windows or higher stress.

6.2. Contribution of shrinkage

A second counter-factual isolates the shrinkage contribution. The GP and GGBFS analyses were repeated with the shrinkage eigenstrain switched off (creep and SCG remaining active). Removing shrinkage lowers the 280-day mid-span deflection from 1.40 to 1.18 mm (GP) and from 1.13 to 0.94 mm (GGBFS) — reductions of about 16.0% and 17.1%. The slightly larger −20 to −21% change reported by the one-at-a-time control (Table 14) corresponds to the Section 6.3 sensitivity baseline, which uses a different mesh–window combination. Restrained drying shrinkage therefore accounts for roughly one-sixth of the total long-term deflection at service load, comparable to the SCG contribution above; the two counter-factuals together separate creep, shrinkage and subcritical-damage in the response.

This contribution is often omitted in related sustained-load models. The subcritical-damage formulation of Wang, Le and Ren [27] and recent refined models for the sustained flexural response of reinforced UHPC members [33,37] concentrate on creep, omit shrinkage, and lack a fully three-dimensional treatment of the reinforcement restraint. Because reinforcement restrains the surrounding concrete's free shrinkage, the resulting self-equilibrated three-dimensional tensile stress, and the tensile damage it drives over time, emerge only when shrinkage is represented in three dimensions. The 16–17% contribution quantified above is exactly the part of the long-term response that creep-only or lower-dimensional models cannot reproduce, the specific advantage of the present three-dimensional model.

The counter-factual was repeated on the Gilbert and Nejadi benchmark of Section 5.5. Fig. 19 compares the full, no-SCG and creep-only predictions against the two beams, and Table 13 decomposes the 300-day deflection. Creep accounts for most growth above the instantaneous value (+3.95 mm for B1a, +3.16 mm for B1b); restrained drying shrinkage adds +1.94 and +2.64 mm; and the subcritical kinetics add +1.13 mm (B1a) and +0.33 mm (B1b), closing the remaining gap onto the measured curve. Restrained shrinkage thus supplies 28–43% of the 300-day time-dependent increment across the two beams — of the same order as creep, and a contribution absent from plain-concrete subcritical frameworks — so at service stress the long-term deflection is governed jointly by creep and restrained shrinkage rather than by creep alone. With shrinkage suppressed the subcritical term alone adds only +0.07 and +0.10 mm, so it is amplified once shrinkage is active, most for the higher-load B1a, as shrinkage-induced tensile stress enlarges the cracked region. The shrinkage-mediated contribution seen in-house is thus reproduced at two further load levels and a different section.

Table 13
Predicted mid-span deflection of each configuration for the Gilbert and Nejadi benchmark beams: 20–300-day error metrics of Eqs. (43)–(46) against the measured response, and the 300-day value, with the measurement for reference.

Configuration	Beam	RMSE (mm)	MAPE (%)	R^2	Bias (mm)	δ_{300} (mm)
Creep only	B1a	2.364	23.41	−4.17	−2.301	8.21
	B1b	1.917	34.02	−3.02	−1.840	4.16
Creep + shrinkage (no SCG)	B1a	1.154	11.85	−0.23	−1.144	10.15
	B1b	0.180	2.88	0.965	−0.096	6.80
Full (creep + shrinkage + SCG)	B1a	0.282	2.52	0.927	−0.233	11.28
	B1b	0.169	2.89	0.969	+0.016	7.12
Test (measured)	B1a	—	—	—	—	11.69
	B1b	—	—	—	—	7.25

6.3. Parameter sensitivity

The robustness of the predictions to the subcritical crack-growth (SCG) parameters was assessed by a one-at-a-time (OAT) study on the in-house beams (15 mm mesh, 268-day window). Each SCG parameter was perturbed about its baseline in turn: the tensile kinetic amplitude A_s^+ was halved and doubled (±100%), the activation sensitivity B_s^+ and the rate exponent k_s^+ changed by ±25%, and the damage threshold d_0^+ raised from 0 to 0.05, with a shrinkage-off control repeated for both the GP and GGBFS concretes. The resulting 268-day mid-span deflections are collected in Table 14 and shown as a tornado plot in Fig. 20. Effect magnitudes $|\Delta\delta|$ are reported throughout for the seven parameter perturbations, as the signs of these sub-3% changes differ between beams and mixes; the shrinkage-off control is signed. Three points emerge. First, the response to the SCG parameters is bounded: the largest single-parameter change is about 8% (GP, driven by d_0^+) and 14% (GGBFS, driven by A_s^+), so no SCG parameter dominates the total deflection and

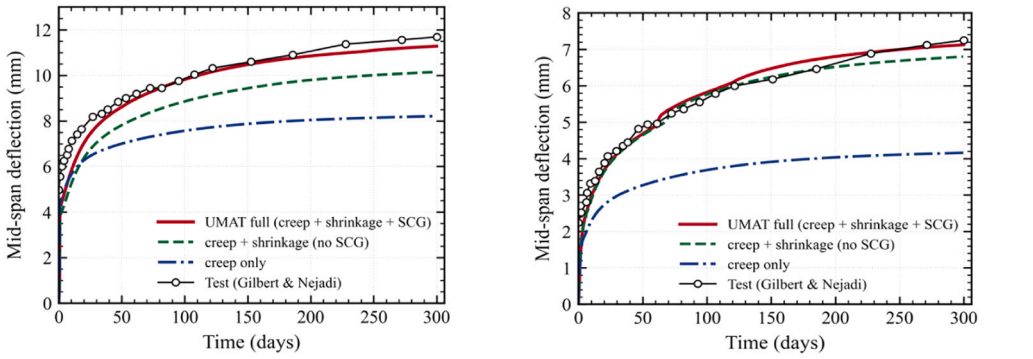


Fig. 19. a. B1a (18.6 kN): mechanism ablation. b. B1b (11.8 kN): mechanism ablation.

Table 14
One-at-a-time SCG parameter sensitivity relative to the baseline (BASE) SCG set: for the GP and GGBFS beams the change in mid-span deflection (Δ%, 268 days, 15 mm mesh), and for the independent Gilbert and Nejadi beams B1a and B1b the deflection and its change (δ_{300}, 300 days, 25 mm mesh). The B1b shrinkage-off row is the converged 20 mm counterfactual of Fig. 20(c); all other rows use the meshes stated above. For the seven SCG-parameter perturbations the magnitude of the change $|\Delta\delta|$ is reported, as the sign of these small (sub-3%) changes varies between beams and mixes with the trade-off of the counteracting mechanisms of Sections 6.1 and 6.2; the shrinkage-off control row is signed (a reduction in every beam).

Variant	Parameter change	GP Δ (%)	GGBFS Δ (%)	B1a δ_{300} (mm)	B1a Δ (%)	B1b δ_{300} (mm)	B1b Δ (%)
Baseline	reference SCG set	—	—	11.267	—	7.127	—
A× 0.5	$A_s^* \times 0.5$	3.2	0.8	11.160	0.95	7.095	0.46
A× 2	$A_s^* \times 2$	2.0	14.4	11.328	0.54	7.161	0.47
B−25%	$B_s^* - 25\%$	7.1	0.9	10.987	2.48	7.025	1.43
B+25%	$B_s^* + 25\%$	2.9	2.6	11.292	0.22	7.212	1.19
k − 25%	$k_s^* - 25\%$	0.3	0.2	11.235	0.28	7.140	0.18
k + 25%	$k_s^* + 25\%$	0.7	0.9	11.229	0.34	7.110	0.24
d_0 = 0.05	d_0^*: 0 → 0.05	8.3	1.2	11.056	1.87	7.096	0.43
Shrinkage off	eigenstrain off (control)	−19.8	−21.3	8.23	−26.9	4.25	−40.3

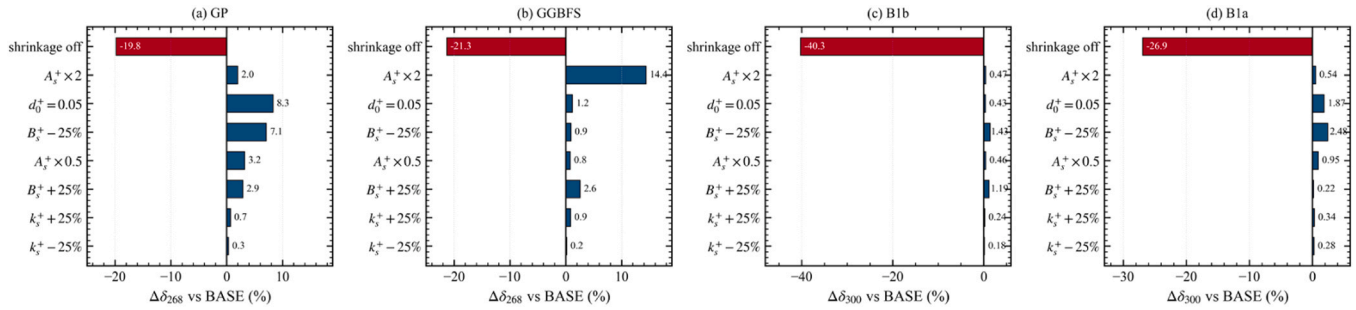


Fig. 20. One-at-a-time sensitivity of the mid-span deflection to the SCG parameters, relative to each baseline (BASE), for (a) the GP and (b) the GGBFS beam (268-day window, 15 mm mesh), and the independent Gilbert and Nejadi beams (c) B1b and (d) B1a (300 days, 25 mm mesh); in each panel the shrinkage-off control (red) is shown for comparison (the B1b control from the converged 20 mm counterfactual, the B1a control on the same 25 mm mesh as its baseline).

the model is not finely tuned to any one of them. Second, the influential parameters differ by mix, B_s^+ and d_0^+ for GP against A_s^+ for GGBFS — the latter strongly asymmetric (halving A_s^+ moves the result by under 1%, indicating saturation at low rates) — reflecting the different instantaneous damage that gates the SCG kinetics. Third, switching drying shrinkage off changes the deflection by −20 to −21%, exceeding any SCG perturbation and confirming that restrained shrinkage is a first-order effect at service load. The small non-monotonic shifts for individual perturbations (for example, both B_s^+ variants of the GP beam lying above the baseline) reflect discrete rearrangements of the smeared crack pattern, not a smooth parametric trend; the bounded envelope, not the sign of any single shift, is the robust finding.

At service stress the SCG term itself thus remains a modest contributor, consistent with the plain-concrete findings of Wang et al. [28]; the contribution here is the three-dimensional framework in which that term interacts with creep and restrained shrinkage.

The same one-at-a-time protocol applied to the independent Gilbert and Nejadi beam B1b (11.8 kN, 25 mm mesh, 300 days; baseline 7.13 mm) shows an even weaker dependence at low sustained stress: halving and doubling A_s^+ change the 300-day deflection by 0.46% and 0.47%, ±25% on B_s^+ by 1.43% and 1.19%, ±25% on k_s^+ by 0.18% and 0.24%, and activating the damage seed ($d_0^+ = 0.05$) by 0.43% — every perturbation at most 1.5% in magnitude, so the benchmark predictions of Section 5.5 are robust to the SCG-parameter uncertainty (Fig. 20(c); Table 14). By contrast, disabling restrained shrinkage removes about 40% of the 300-day deflection (from 7.12 to 4.25 mm), confirming — as for the GP and GGBFS beams (Section 6.2) — that restrained shrinkage, not the SCG term, is the first-order contributor at service load.

At the higher B1a service load (18.6 kN, 25 mm mesh, 300 days; baseline 11.27 mm) the same perturbations produce generally larger but still bounded changes in the 300-day deflection: $A_s^+ \times 0.5$ 0.95%, $A_s^+ \times 2$ 0.54%, $B_s^+ - 25\%$ 2.48%, $B_s^+ + 25\%$ 0.22%, $k_s^+ - 25\%$ 0.28%, $k_s^+ + 25\%$ 0.34%, $d_0^+ = 0.05$ 1.87%. The strongest single-parameter effect ($B_s^+ - 25\%$, a 2.48% change) is about 1.7 times the corresponding B1b response (1.43%), so raising the sustained load from 11.8 to 18.6 kN amplifies the SCG-parameter sensitivity while keeping every change within about 2.5%. This load-dependence follows the stress-ratio driving of the subcritical branch (Section 6.2): the predictions stay robust to SCG-parameter uncertainty across both service-load levels. Switching drying shrinkage off lowers the B1a prediction from 11.27 to 8.23 mm (−26.9%), a proportionally smaller shrinkage contribution than for B1b (−40.3%), consistent with the higher sustained load shifting the long-term increment toward creep and subcritical growth (Fig. 20(d); Table 14).

7. Conclusions

A new method for the three-dimensional creep analysis of concrete under sustained service loading has been developed, coupling a CDPM1-type plasticity surface, an energy-release-rate damage law, a Dirichlet-series creep compliance fitted to the AS 3600 creep coefficient, and a subcritical damage-growth term for the time-dependent stiffness loss below the short-term strength. The ABAQUS UMAT combines an implicit effective-stress return mapping and an analytical consistent tangent with a staggered scalar SCG update — the operator-split practice of existing subcritical models — integrated by backward Euler for stability at day-scale increments. To the authors' knowledge this is the first structural-scale three-dimensional creep-analysis method to couple subcritical damage growth, creep and restrained shrinkage in a single plastic-damage UMAT.

The principal findings are as follows.

(i) The effective-stress decomposition keeps the plastic return mapping, damage update, and creep convolution algorithmically independent, reducing the stress update to a 3 × 3 Newton–Raphson system with an analytical Jacobian, while the crack-band regularisation ensures mesh-objective softening energy dissipation at the constitutive level.

(ii) The mesh-sensitivity study shows that the global deflection response and damage-zone envelope are robust as the element size is reduced from 20 to 10 mm, while localised crack bands shift with refinement, as expected for smeared continuum damage.

(iii) The long-term analysis keeps the FEA mid-span deflection inside the GP2/GP3 experimental band over the 280 day window, with RMSE of 0.086–0.098 mm, MAPE below 6.22%, R^2 above 0.847, and bias within 0.054 mm across the three meshes—comparable to the specimen-to-specimen scatter (mean GP3–GP2 spread 0.035 mm).

(iv) The counter-factual study indicates that, for the GP beams tested here, the subcritical damage term is the dominant mechanism behind the decelerating long-term branch: disabling the SCG kinetics raises the RMSE to 0.232 mm and the MAPE to 14.48%, lowers R^2 to 0.138, and produces a uniformly negative bias on every mesh; linear creep alone cannot reproduce the observed deflection growth. The independent-benchmark decomposition further attributes 28–43% of the time-dependent increment to restrained shrinkage, so serviceability deflection is governed jointly by creep and restrained shrinkage, with the subcritical term acting within — and amplified by — the shrinkage-enlarged cracked region. For the GGBFS mix the with- and no-SCG predictions remain close, so this conclusion is not generalised beyond the GP case.

(v) Agreement for both GP and GGBFS beams, a mesh-robust global response, and the counter-factual SCG study support the model for serviceability assessment under sustained flexural loading within the scope of the configurations examined here — the two in-house mixes together with an independent published sustained-load benchmark that adds a second beam geometry, a different reinforcement layout, and two further load levels. Crack-pattern comparisons remain qualitative, with observed cracks and simulated damage both concentrating in the constant-moment region.

Within the scope of the configurations examined — two beams per mix at a single geometry, reinforcement layout and service-load level over a window of up to 280 days, extended by the independent benchmark — the main limitations are the literature-adopted SCG parameters, the code-based creep–shrinkage representation and the qualitative crack-field comparison, with local damage bands that remain mesh-dependent over the 10–20 mm range. Independent calibration of the subcritical kinetics for the present mixes, quantitative crack-width monitoring by DIC and automated crack tracking building on the preliminary work of Appendix B, finer spatial and temporal discretisations, validation campaigns spanning further concrete strengths and reinforcement ratios, and coupling with an internal-relative-humidity–driven shrinkage description [38–40], extended to incorporate temperature effects on moisture transport and shrinkage, are natural extensions.

CRediT authorship contribution statement

Yuan Dong: Writing – original draft, Visualization, Validation, Software, Formal analysis, Data curation, Conceptualization. **Jun Li:** Writing – review & editing, Supervision, Methodology, Formal analysis, Conceptualization. **Shami Nejadi:** Writing – review & editing, Supervision, Conceptualization. **Arnaud Castel:** Writing – review & editing, Supervision, Project administration, Funding acquisition, Conceptualization.

Funding

This research was funded by BG&E and the Cooperative Research Centre (CRC) SmartCrete Project “Refining Design Deformation Predictions by Improving Concrete Volume Stability Assessment (22. PP.0151)”.

Declaration of Competing Interest

The authors declare that they have no known competing financial interests or personal relationships that could have appeared to influence the work reported in this paper.

Appendix A. . UMAT algorithmic flow

Fig. A1 summarises one constitutive update at a Gauss point. The steps below follow the boxes of the flowchart from top to bottom so the implementation can be reproduced directly.

Step 1 — state recovery. The converged effective stress, the Dirichlet creep history variables W_i, the hardening variable κ_p, the instantaneous damage variables $\omega^{\pm}_{inst}$, and the subcritical variables $d^{\pm}_c$ are read from the Abaqus state array (STATEV).

Step 2 — creep and shrinkage increment. The recursive Dirichlet update of Eqs. (29)–(30) advances the creep strain over the increment, and the AS 3600 shrinkage eigenstrain is added; both are subtracted from the total strain increment to give the mechanical strain increment of Eq. (23).

Step 3 — elastic trial. A trial effective stress is computed from the mechanical strain increment with the undamaged elastic moduli (Eq. (31)).

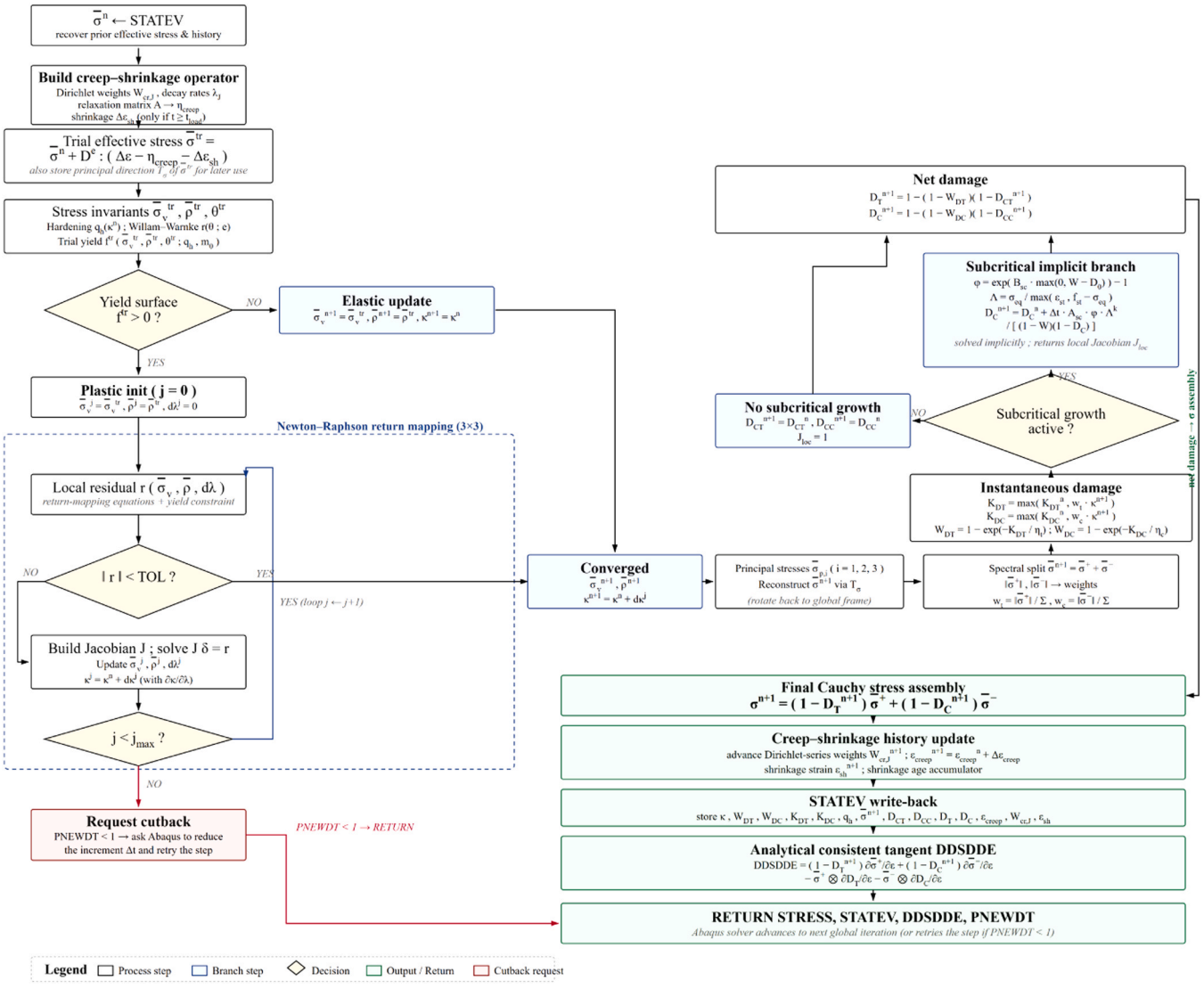
Step 4 — plastic return mapping. The trial state is checked against the Menétrey–Willam yield function; if it is violated, the 3×3 residual system of Eq. (35) is solved by Newton–Raphson iteration with the analytical Jacobian of Eq. (36), and the hardening variable κ_p is updated at convergence.

Step 5 — instantaneous damage update. The damage history envelopes of Eq. (38) are advanced and the instantaneous damage components $\omega^{\pm}_{inst}$ follow from the exponential softening law of Eq. (39), with the crack-band scaling of Eq. (16) applied through the element length CELENT.

Step 6 — subcritical damage update. The SCG rate law is integrated implicitly over the increment: the scalar backward-Euler residual of Eq. (40) is solved for $d^{\pm}_c$ by a local Newton iteration with the analytical tangent of Eq. (41).

Step 7 — stress recovery. The instantaneous and subcritical components are combined through the probabilistic union of Eq. (20); the nominal stress follows from Eq. (1b) with the spectral split of Eq. (22).

Step 8 — tangent and state storage. The analytical consistent tangent is assembled and returned together with the updated state array. If either local Newton loop fails to converge within j_{max} iterations, the increment is abandoned and PNEWDT < 1 asks the solver to retry with a smaller time step.



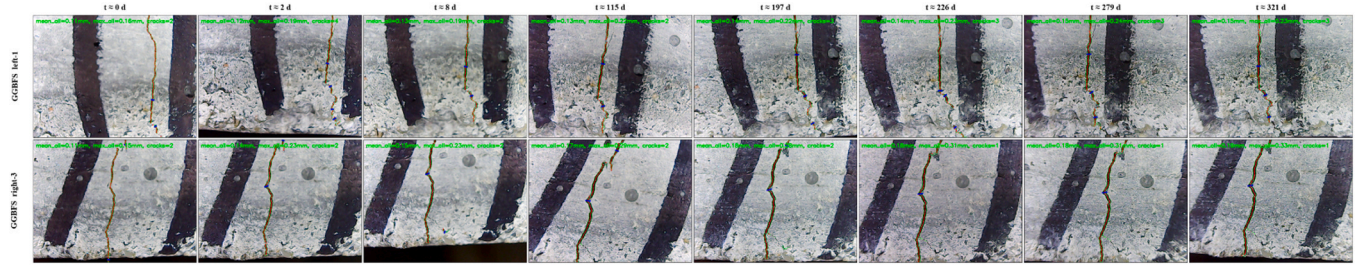
Appendix Fig. A1. UMAT flowchart

Table 15
Static (short-term) constitutive and solver parameters of the UMAT for the GP and GGBFS concretes, as set in the subroutine source. The subcritical parameters are listed in Table 1; the creep and shrinkage inputs are the AS 3600 fits of Section 2.4 calibrated by the measured data of Section 4.2

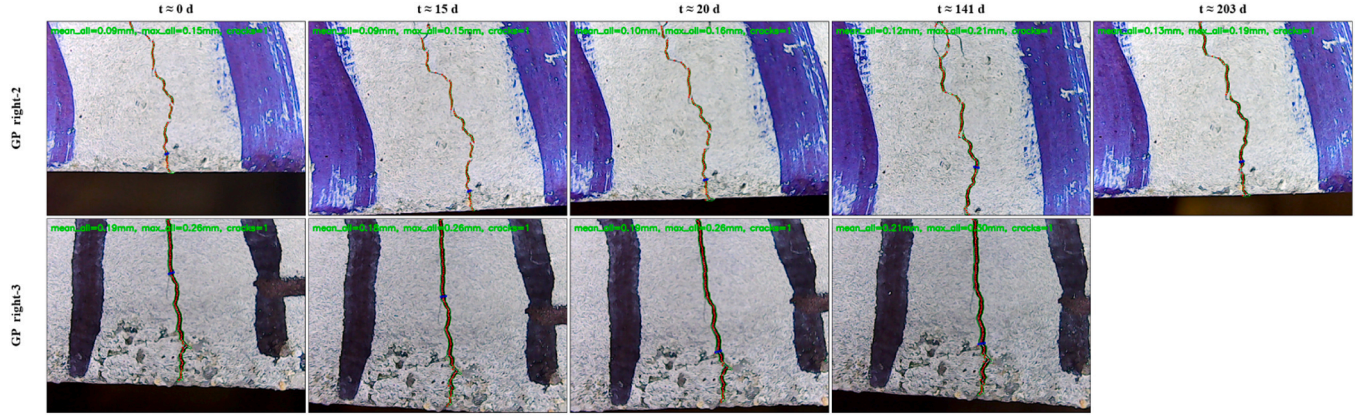
Parameter	UMAT constant	GP	GGBFS	Basis
Elastic modulus E (MPa)	EM	30 000	36 000	Measured (Section 4.2)
Poisson ratio ν	VM	0.20	0.20	Adopted
Compressive strength f_c (MPa)	FCU	44.4	60.0	Measured, 28-day average (Table 4)
Tensile strength f_t (MPa)	FTU	3.0	3.4	Adopted (framework)
Biaxial ratio f_b/f_c	FBU/FCU	1.16	1.16	CDPM1
Initial hardening q_{h0}	QH0	1/3	1/3	CDPM1
Hardening constants A_h, B_h, C_h, D_h	AAH, BBH, CCH, DDH	0.08, 0.003, 2.0, 10^{-6}	0.08, 0.003, 2.0, 10^{-6}	CDPM1
Softening strain ε_f	EF	1.0×10^{-4}	1.0×10^{-4}	Crack-band scaled (Eq. 16)
Fracture energy G_f (N/mm)	GF	0.12	0.10	Calibrated (first-loading response)
Compressive damage shape D_f	DF	0.85	0.85	CDPM1
Ductility factor x_s	XS_DUC	10.0	10.0	Calibrated (Section 2.2)
Damage cap d_{max}	DMAX_NET	0.9999	0.9999	State-variable bound (Section 5.5)
Residual-stiffness factor k_{reg}	KREG_DMG	$10^{-4}\,f_t$	$10^{-4}\,f_t$	Regularisation
Viscoplastic viscosity η_{vp}	ETA_VP	10^{-3}	10^{-3}	Perzyna regularisation
Per-increment damage limits ΔD_c, $\Delta\omega_t$	DDCMAX, DWDMAX	0.05, 0.05	0.05, 0.10	Rate limiter (Section 3.4)
Local Newton: tolerance / max iterations / strain sub-increment	TOL, JNRMAX, DEPS_MAX_SUB	10^{-8}, 50, 5×10^{-4}	10^{-8}, 50, 5×10^{-4}	Solver settings

Appendix B. . Crack-development monitoring

Crack development at the beam soffit was monitored throughout the sustained-load period with a fixed-focus macro camera positioned at fixed reference locations, so that the same crack could be re-imaged at a constant working distance and magnification at each inspection. The same camera and procedure were used for the GGBFS beam (Appendix Fig. B1) and the GP beam (Appendix Fig. B2). Dedicated crack-imaging equipment was not available at the very start of the sustained-loading period, so imaging began only once it could be set up; the photographic record is therefore partial and does not cover the earliest ages at every location, with fuller coverage for the GGBFS beam than for the GP beam. Each photograph is overlaid with an automated crack trace and a preliminary width estimate obtained from a U-Net segmentation; these annotations are reported here only to illustrate the monitoring capability. The images confirm qualitatively that, for both mixes, the flexural cracks in the constant-moment region form early and then grow slowly under sustained load, consistent with the simulated damage fields of Section 5. A quantitative analysis of the crack-width evolution and its validation against the predicted damage field are left to future research (Section 7).



Appendix Fig. B1. Crack development at two soffit locations of the GGBFS beam (rows) at successive ages under sustained load (columns); fixed-focus macro camera, with automated crack trace and preliminary width annotation



Appendix Fig. B2. Crack development at two soffit locations of the GP beam (rows) at successive ages under sustained load (columns); same fixed-focus macro camera and procedure as the GGBFS beam

Data Availability

Data will be made available on request.

References

[1] Bažant ZP, Jirásek M. Creep and Hygrothermal Effects in Concrete Structures. Dordrecht, The Netherlands: Springer; 2018. https://doi.org/10.1007/978-94-024-1138-6.
[2] Gilbert RI, Ranzi G. Time-Dependent Behaviour of Concrete Structures. London, U. K: Spon Press; 2011.
[3] Bažant ZP, Hubler MH, Yu Q. Excessive creep deflections: an awakening. Concr Int 2011;33(8):44–6.
[4] Gilbert RI. Creep and shrinkage induced deflections in RC beams and slabs. Shrinkage and Creep of Concrete. Farmington Hills, MI, USA: American Concrete Institute; 2005. p. 1–14.
[5] Lubliner J, Oliver J, Oller S, Oñate E. A plastic-damage model for concrete. Int J Solids Struct 1989;25(3):299–326. https://doi.org/10.1016/0020-7683(89)90050-4.
[6] Lee J, Fenves GL. Plastic-damage model for cyclic loading of concrete structures. J Eng Mech 1998;124(8):892–900. https://doi.org/10.1061/(ASCE)0733-9399(1998)124:8(892).
[7] Grassl P, Xenos D, Nyström U, Rempling R, Gylltoft K. CDPM2: A damage-plasticity approach to modelling the failure of concrete. Int J Solids Struct 2013;50(24):3805–16. https://doi.org/10.1016/j.ijsolstr.2013.07.008.
[8] Wu JY, Li J, Faria R. An energy release rate-based plastic-damage model for concrete. Int J Solids Struct 2006;43(3–4):583–612. https://doi.org/10.1016/j.ijsolstr.2005.05.038.
[9] Grassl P, Jirásek M. Damage-plastic model for concrete failure. Int J Solids Struct 2006;43(22–23):7166–96. https://doi.org/10.1016/j.ijsolstr.2006.06.032.
[10] Mazars J, Pijaudier-Cabot G. Continuum damage theory: Application to concrete. J Eng Mech 1989;115(2):345–65. https://doi.org/10.1061/(ASCE)0733-9399(1989)115:2(345).
[11] Mazzotti C, Savoia M. Nonlinear creep damage model for concrete under uniaxial compression. J Eng Mech 2003;129(9):1065–75. https://doi.org/10.1061/(ASCE)0733-9399(2003)129:9(1065).
[12] Ren X, Wang Q, Ballarini R, Gao X. Coupled creep-damage-plasticity model for concrete under long-term loading. J Eng Mech 2020;146(5):04020027. https://doi.org/10.1061/(ASCE)EM.1943-7889.0001748.
[13] ACI Committee 209, Prediction of Creep, Shrinkage, and Temperature Effects in Concrete Structures, ACI 209R-92. Farmington Hills, MI, USA: American Concrete Institute, 1992.
[14] fédération internationale du béton (fib), fib Model Code for Concrete Structures 2010. Berlin, Germany: Ernst & Sohn, 2013, doi: 10.1002/9783433604090.
[15] 2018. Concrete Structures, AS 3600Standards Australia2018. Sydney, NSW, AustraliaStandards Australia.
[16] Bažant ZP, Baweja S. Creep and shrinkage prediction model for analysis and design of concrete structures — Model B3. Mater Struct 1995;28(6):356–65. https://doi.org/10.1007/BF02473152.
[17] Wendner R, Hubler MH, Bažant ZP. Model B4 for creep, drying shrinkage and autogenous shrinkage of normal and high-strength concretes with multi-decade applicability. Mater Struct 2015;48(4):753–70. https://doi.org/10.1617/s11527-014-0485-2.

[18] Bažant ZP, Hauggaard AB, Baweja S, Ulm F-J. Microprestress-solidification theory for concrete creep. I: Aging and drying effects. J Eng Mech 1997;123(11):1188–94. https://doi.org/10.1061/(ASCE)0733-9399(1997)123:11(1188).
[19] Castel A, Vidal T, François R. Finite-element modeling to calculate the overall stiffness of cracked reinforced concrete beams. J Struct Eng 2012;138(7):889–98. https://doi.org/10.1061/(ASCE)ST.1943-541X.0000520.
[20] Castel A, Gilbert RI, Ranzi G. "Instantaneous stiffness of cracked reinforced concrete including steel-concrete interface damage and long-term effects,". J Struct Eng (ASCE) 2014;140(6):04014021. https://doi.org/10.1061/(ASCE)ST.1943-541X.0000954.
[21] Fragiacomo M, Amadio C, Macorini L. "Finite element model for collapse and long-term analysis of steel-concrete composite beams,". J Struct Eng (ASCE) 2004;130(3):489–97. https://doi.org/10.1061/(ASCE)0733-9445(2004)130:3(489).
[22] Li S, Yang Y, Pu Q, Yang D, Sun B, Li X. Three-dimensional nonlinear creep and shrinkage effects of a long-span prestressed concrete box girder bridge. Struct Concr 2019;20(2):638–49. https://doi.org/10.1002/suco.201800148.
[23] Noushini A, Castel A, Gilbert RI. Creep and shrinkage of synthetic fibre-reinforced geopolymer concrete. Mag Concr Res 2019;71(20):1070–82. https://doi.org/10.1680/jmacr.18.00053.
[24] Charles RJ. Static fatigue of glass. J Appl Phys 1958;29(11):1549–53. https://doi.org/10.1063/1.1722992.
[25] Atkinson BK. Subcritical crack growth in geological materials. J Geophys Res 1984;89(B6):4077–114. https://doi.org/10.1029/JB089iB06p04077.
[26] Krausz AS, Krausz K. Fracture Kinetics of Crack Growth. Dordrecht, The Netherlands: Kluwer; 1988. https://doi.org/10.1007/978-94-009-1381-3.
[27] Wang Q, Le J-L, Ren X. Numerical modelling of delayed damage and failure of concrete structures under sustained loading. Eng Struct 2022;252:113568. https://doi.org/10.1016/j.engstruct.2021.113568.
[28] Wang Q, Li J, Ren X. "A subcritical microcrack informed creep-damage model for quasi-brittle materials,". Comput Geotech 2022;141:104501. https://doi.org/10.1016/j.compgeo.2021.104501.
[29] Li J, Ren X. Stochastic damage model for concrete based on energy equivalent strain. Int J Solids Struct 2009;46(11–12):2407–19. https://doi.org/10.1016/j.ijsolstr.2009.01.024.
[30] Wang Q. Time-dependent damage model for quasi-brittle materials. Shanghai, China: Coll. Civil Eng., Tongji Univ.; 2023.
[31] Chianeh SM, Shen L, Dias-da-Costa D. A creep damage model for cracked concrete accounting for the rate of crack opening in a discrete strong discontinuity framework. Eng Fract Mech 2025;315:110801. https://doi.org/10.1016/j.engfracmech.2025.110801.
[32] Nie Y, Xie T, Zhao X-Y. A 3D damage plastic model incorporating low-cycle fatigue effects towards predicting concrete structure failure under cyclic loading. Eng Fract Mech 2025;316:110905. https://doi.org/10.1016/j.engfracmech.2025.110905.
[33] Zhang Z, Leng J, Bian X, Xie T, Xu T. A refined model for the flexural behavior of reinforced UHPC members under sustained loading. J Build Eng 2024;93:109853. https://doi.org/10.1016/j.jobe.2024.109853.
[34] Dong Y, Li J, Nejadi S, Xu T, Castel A. "Time-dependent numerical modelling of conventional and geopolymer concrete beams serviceability,". J Build Eng 2026;118:114971. https://doi.org/10.1016/j.jobe.2025.114971.
[35] Bažant ZP, Wu ST. Dirichlet series creep function for aging concrete. J. Eng. Mech. Div., 99. ASCE; 1973. p. 367–87. https://doi.org/10.1061/JMCEA3.0001741.
[36] Nejadi S. Time-dependent cracking and crack control in reinforced concrete structures. New South Wales, Sydney, NSW, Australia: School of Civ. and Environ. Eng., Univ. of; 2005. https://doi.org/10.26190/unsworks/22523.
[37] Zhang Z. Compressive creep behaviour of UHPC over the full stress range and methods for creep-effect analysis. Chengdu, China: School of Civil Eng., Southwest Jiaotong Univ.; 2023.
[38] Chen X, Zhang H, Zhou C, Geng Y, Wang Y-Y. Tests and theoretical prediction model for RH evolution in recycled aggregate concrete accounting for the porous physical properties of recycled aggregates. J Mater Civ Eng 2025;37(4):04025053. https://doi.org/10.1061/JMCEE7.MTENG-19321.
[39] Chen X, Wang Y-Y, Zhou C, Geng Y, Zhang H. An RH-based non-uniform shrinkage prediction model considering the environmental humidity fluctuations and decorative layer sealing effect for steel-recycled aggregate concrete composite slabs. Constr Build Mater 2025;474:141087. https://doi.org/10.1016/j.conbuildmat.2025.141087.
[40] Chen X, Zhang H, Wang Y-Y, Dai H, Fan L, Geng Y. Long-term performance of steel-recycled aggregate concrete continuous composite beams considering the influence of installing decorative layers. Eng Struct 2025;339:120569. https://doi.org/10.1016/j.engstruct.2025.120569.